

A simple multistage closed-(box+reservoir) model of chemical evolution

R. Caimmi*

October 21, 2010

Abstract

Simple closed-box (CB) models of chemical evolution are extended on two respects, namely (i) simple closed-(box+reservoir) (CBR) models allowing gas outflow from the box into the reservoir (Hartwick 1976) or gas inflow into the box from the reservoir (Caimmi 2007) with same composition as the preexisting gas and rate proportional to the star formation rate, and (ii) simple multistage closed-(box+reservoir) (MCBR) models allowing different stages of evolution characterized by different inflow or outflow rates. In any case, the stellar initial mass function is assumed to be universal, and mass conservation holds for the whole system (box+reservoir) while it is violated for each subsystem (box and reservoir). The theoretical differential oxygen abundance distribution (TDOD) predicted by the model, under the assumption of instantaneous recycling, is a continuous broken line, where outflow and moderate inflow rates are represented by negative slopes, steady inflow rates by null slopes, and strong inflow rates by positive slopes. Then an application is made to a special stellar system resembling the inner Galactic halo. To this aim (a) a fictitious sample is built up from two distinct samples (Ryan and Norris 1991; Schörck et al. 2009) and taken as representative of the inner Galactic halo, and (b) different $[O/H]$ - $[Fe/H]$ empirical relations are deduced from different samples (Rich and Boesgaard 2009; Fabbian et al. 2009;

**Astronomy Department, Padua Univ., Vicolo Osservatorio 3/2, I-35122 Padova, Italy*
email: roberto.caimmi@unipd.it fax: 39-049-8278212

Schmidt et al. 2009) related to different methods, and two of them are selected for determining the empirical differential oxygen abundance distribution (EDOD) with regard to the fictitious sample. In both cases the EDOD is represented, to an acceptable extent, as a continuous broken line. The slopes and the intercepts of the regression lines are determined, and then used as input parameters to MCBR models with fiducial values assigned to the remaining input parameters. Output parameters are the gas mass fraction and the star mass fraction at the end of each evolutionary stage. If the inner halo and the metal-poor bulge (after the inflow stage) are represented by the box and the reservoir, respectively, then the inner halo fractional mass (normalized to the halo) is comparable with, or exceeds by a factor up to 4, the metal-poor bulge fractional mass (normalized to the bulge), for current estimates of the halo-to-bulge mass ratio of about 0.05-0.10. On the other hand, quantitative results cannot be considered for applications to the inner Galactic halo, unless selection effects and disk contamination are removed from halo samples, and discrepancies between different oxygen abundance determination methods are explained.

keywords - *galaxies: evolution* - *stars: formation; evolution*.

1 Introduction

The empirical metallicity distributions of long-lived stars of different populations, constrain models for the formation and the evolution of the Galaxy. Simple closed-box (CB) models make a useful tool in the description of galactic chemical evolution. The original formulation (Searle and Sargent 1972; Pagel and Patchett 1975) relies on instantaneous recycling and homogeneous mixing approximations i.e. gas from dying stars is instantaneously returned to and homogeneously mixed with the interstellar medium. In addition, (1) a null star mass fraction and a null metal abundance are taken as initial values, and (2) mass conservation is assumed to hold, which implies no gas outflow from the box or inflow into the box.

Simple CB models may be extended in many respects, such as nonzero initial metal abundance (prompt initial enrichment) and/or star mass fraction (Truran and Cameron 1971), inhomogeneous mixing (Caimmi 2000 + erratum 2001a, hereafter quoted together as C00; Caimmi 2001b, hereafter quoted as C01), and gas outflow (Hartwick 1976, hereafter quoted as H76) or inflow (Caimmi 2007, hereafter quoted as C07) with same composition as the preexisting gas and rate proportional to the star formation rate. Formulations implying more extreme changes, such as reject of instantaneous

recycling and unconditioned gas outflow or inflow, can no longer be considered as “simple” models.

The existence of a G-dwarf problem i.e. detection of too few metal deficient G dwarf (or, more generally, of a selected spectral type) with respect to that which could be expected from simple CB models of chemical evolution (e.g., Searle and Sargent 1972; Pagel and Patchett 1975; Haywood 2001) was first established in the solar neighbourhood (van den Bergh 1962; Schmidt 1963). Although in a less extreme form, a G-dwarf problem appears to exist both in the halo (e.g., H76; Prantzos 2003) and in the bulge (e.g., Ferreras et al. 2003). In addition, a G-dwarf problem has been recognized in both bulge-dominated and disk-dominated galaxies (Henry and Worthey 1999), which is consistent with the idea that the G-dwarf problem is universal (Worthey et al. 1996).

According to current Λ CDM cosmological scenarios, galaxies were largely built out of disrupted smaller subunits (dSph galaxies whose surviving cores could be massive globular clusters). A similar process is presently occurring on a larger scale: a central bulge (a cD galaxy) is accreting in galaxy clusters, at the expense of infalling smaller galaxies. In this view, a universal G-dwarf problem appears to be closely related to the initial assembling stage of galactic evolution.

With regard to the Galaxy, the empirical differential oxygen abundance distribution (EDOD) shows that (i) at least two different stages of (chemical) evolution exist, and (ii) each stage can be described using an extended simple CB model, for both the inner halo (C07), the bulge (C07), the thick disk (Caimmi and Milanese 2009, hereafter quoted as CM09), and the thin disk (CM09). In particular, the earlier stage is marked by an initially increasing EDOD.

The advantage of the EDOD, $\psi = \log[\Delta N/(N\Delta\phi)]$ ¹, on the oxygen abundance distribution, $\Psi = \Delta N/N$, is that the theoretical differential oxygen abundance distribution (TDOD) predicted by extended simple CB models is a straight line on the $(O\phi\psi)$ plane, which provides a more sensitive test (Pagel 1989; Malinie et al. 1993; Rocha-Pinto and Maciel 1996; C00; C01; C07; Caimmi 2008; CM09).

As shown in recent attempts (Carollo et al. 2007, 2010), the Galactic halo may be divided into two structural components, namely (1) an inner spheroid with axes, $a \approx 15$ kpc, $c \approx 10$ kpc, which exhibits a modest prograde rotation and a metallicity peak at $[\text{Fe}/\text{H}] \approx -1.6$, and (2) an outer sphere with radius,

¹Caption of symbols: $\phi = Z_{\text{O}}/(Z_{\text{O}})_{\odot}$ is the oxygen abundance normalized to the solar value, N is the population of the sample under consideration, and ΔN is the number of sample objects within a bin centered in ϕ and bounded at $\phi \pm \Delta\phi/2$.

$R \approx 20$ kpc, which exhibits a clear retrograde net rotation and a metallicity peak at $[\text{Fe}/\text{H}] \approx -2.2$. In addition, the inner halo population dominates within its own volume, while the outer halo population includes a larger fraction of low-metallicity ($[\text{Fe}/\text{H}] < -2.0$) stars than does the inner halo population.

For a component of orbital motion measured with respect to the Local Standard of Rest, $V < 200 \text{ km s}^{-1}$, the distribution of $[\text{Fe}/\text{H}]$ appears similar to what in the past was considered “the halo”, with a single metallicity peak at $[\text{Fe}/\text{H}] \approx -1.6$ (Carollo et al. 2007, Fig. 2), which implies the inner halo population is dominant in the related sample. A similar trend is exhibited by the metallicity distribution inferred from an earlier attempt (Ryan and Norris 1991, hereafter quoted as RN91, Fig. 5c), and the related sample (hereafter quoted as the RN91 sample) can also be considered as representative of the inner halo. In both cases, data are biased towards low metallicities, $[\text{Fe}/\text{H}] < -3.0$.

The inner halo low-metallicity tail has been determined using data from the Hamburg/ESO survey (Schörck et al. 2009, hereafter quoted as H V, Fig. 11), but the related sample (hereafter quoted as the H V sample) is biased towards higher metallicities, $[\text{Fe}/\text{H}] > -3.0$, and extremely low metallicities, $[\text{Fe}/\text{H}] < -4.2$. In the comparison of the empirical with the theoretical metallicity distribution, selection effects must be taken into account. Accordingly, each theoretical metallicity distribution under consideration has to be converted into its counterpart as it would be observed by applying the metal-poor star selection criteria used in the survey (H V).

If, on the other hand, the H V sample is dominated by the inner halo population, a correction for the above mentioned selection effects is expected to yield a metallicity distribution with a single peak at $[\text{Fe}/\text{H}] \approx -1.6$, similar to its counterpart related to earlier samples (RN91; Carollo et al. 2007, Fig. 2, $V < 200 \text{ km s}^{-1}$). In fact, the metallicity distributions related to the RN91 and H V sample can be adjusted to match in the range, $-3.4 < [\text{Fe}/\text{H}] < -2.6$, where selection effects are negligible (H V, Figs. 11, 12).

The Milky Way inner halo offers a unique opportunity to construct the star formation and mass assembly history of a galactic inner halo, hence providing a unique benchmark for theories of galaxy formation and evolution. To this aim, the sample used has to be complete at least for a wide range of metallicity. In the case under discussion, $-3.6 < [\text{Fe}/\text{H}] < -2.8$ for the H V sample and $-3.4 < [\text{Fe}/\text{H}] < -1.0$ for the RN91 sample. The remaining ranges are affected by various biases, mainly due to the occurrence of selection effects for the low-metallicity tail above a threshold (H V) and disk contamination for the high-metallicity tail (RN91, H V).

The metallicity distribution of the inner halo can be deduced from a

fictitious sample (hereafter quoted as the fs10 sample) within the range, $-4.2 < [\text{Fe}/\text{H}] < +0.2$, under a number of restrictive but reasonable assumptions, namely (i) the HV sample is representative of the inner halo within the range, $-4.2 < [\text{Fe}/\text{H}] < -3.0$; (ii) the RN91 sample is representative of the inner halo within the range, $-2.8 < [\text{Fe}/\text{H}] < +0.2$; (iii) the HV and RN91 samples are equally representative (even if related to different populations) of the inner halo within the range, $-3.0 \leq [\text{Fe}/\text{H}] \leq -2.8$.

In absence of direct $[\text{O}/\text{H}]$ evaluations, the EDOD related to the fs10 sample can be deduced by use of a $[\text{O}/\text{H}]-[\text{Fe}/\text{H}]$ empirical relation which, on the other hand, is strongly dependent on both the selection of spectroscopic oxygen lines and the choice of the model, as shown in recent attempts (Ramirez et al. 2007; Rich and Boesgaard 2009, hereafter quoted as RB09; Fabbian et al. 2009, hereafter quoted as Fal09; Schmidt et al. 2009, hereafter quoted as Sal09) where earlier attempts are quoted (for further insight refer to the proceedings edited by Barbuy et al. 2001). The discrepancy between $[\text{O}/\text{H}]-[\text{Fe}/\text{H}]$ empirical relations, deduced using different methods and different models, still remains large. For this reason, the TDOD should be fitted to the EDOD related to two different $[\text{O}/\text{H}]-[\text{Fe}/\text{H}]$ empirical relations, as done in previous papers (C01; C07; Caimmi 2008; CM09).

Simple CB models of chemical evolution were first extended allowing for gas outflow (H76) and later for moderate gas inflow, with same metal abundance as in the preexisting gas, yielding negative TDOD slopes in the $(\text{O}\phi\psi)$ plane. On the other hand, the low-metallicity tail of the EDOD is fitted to a straight line with positive slope for both the halo (C07), the bulge (C07), the thick disk (CM09), and the thin disk (CM09), which is achieved by extending simple CB models to strong gas inflow with same metal abundance as the preexisting gas.

In this view, different stages of evolution are related to different domains in the normalized oxygen abundance, $(\phi_U)_i \leq \phi \leq (\phi_U)_f$, where the EDOD is fitted to a regression line, $\psi = a_U \phi + b_U$, with slope, a_U , and intercept, b_U ($U = \text{I, II, ...}$, is the stage considered, beginning and ending at i and f configurations, respectively). For reasons of continuity, the final values of parameters related to a selected stage must necessarily coincide with the corresponding initial values related to the next stage, with the exception of the outflow or inflow rate, which can be deduced from the EDOD. Accordingly, the knowledge of present values allows the calculation of past values, in the light of the model, getting insight on the formation and evolution of the system under consideration.

In summary, the current paper is aimed to the following main points: (i) metallicity distribution related to a fictitious sample (fs10), supposed to be representative of the inner halo (subsection 2.1); (ii) choice of two different

[O/H]-[Fe/H] empirical relations deduced from recent samples (RB09, Fal09, Sal09) (subsection 2.2); (iii) EDOD determination from the fs10 sample by use of the above mentioned [O/H]-[Fe/H] empirical relations (subsection 2.3); (iv) formulation of extended simple CB models, namely (a) simple CBR models, allowing for gas outflow or inflow with same metal abundance as the preexisting gas, and (b) simple MCBR models, allowing for different stages of evolution (subsections 3.1, 3.2 and 3.4); (v) determination of the best fitting TDOD to the EDOD inferred from the fs10 sample (subsection 3.3); (vi) application to a special stellar system resembling the inner Galactic halo (subsection 3.5). In addition, the discussion and the conclusion make the subject of subsection 3.6 and section 4, respectively.

2 Data and inferred quantities

The following ingredients are necessary for the determination of the EDOD (in particular, related to the inner Galactic halo), from which input parameters of a selected model are deduced: (i) a representative sample; (ii) a related [Fe/H] distribution; (iii) a [O/H]-[Fe/H] empirical relation. Each point shall be separately dealt with in the forthcoming subsections.

2.1 Building up a fictitious sample (fs10)

In building up a fictitious sample (the fs10 sample) of inner halo stars, two different samples shall be considered, namely the RN91 sample ($N = 372$) of kinematically selected halo subdwarfs and the HV sample ($N = 3439$) of metal-poor stars selected from the Hamburg/ESO objective prism survey. More specifically, the HV sample has been determined from a subsample ($N = 1638$) with available spectroscopic follow-up observations, by means of scaling to the full parent sample ($N = 3439$). For further details refer to the parent paper (HV). The RN91 sample can be considered as complete within the range, $-3.4 < [\text{Fe}/\text{H}] < -1.0$. At different abundance the sample is incomplete and suffers contamination from disk stars at the high-metallicity tail, $[\text{Fe}/\text{H}] \geq -1.0$. The HV sample can be considered as complete within the range, $-4.2 < [\text{Fe}/\text{H}] < -2.8$. At different abundance the sample is incomplete and suffers both selection effects ($[\text{Fe}/\text{H}] > -2.8$) and contamination from disk stars ($[\text{Fe}/\text{H}] > -2.0$).

Contamination from outer halo stars also exists in both samples, but the effect is expected to be negligible. In fact, the inner halo dominates within a spheroid centered on the Galactic centre, with equatorial plane coinciding with the Galactic plane, and semiaxes $(a, c) = (15, 10)$ kpc (Carollo et al.

2007). On the other hand, both the RN91 and H V sample are made mainly of stars placed within the above mentioned spheroid. Then the contamination from outer halo stars is expected to be appreciable only at low ($[\text{Fe}/\text{H}] < -2.0$) metal abundances (Carollo et al. 2007).

The metallicity distribution from the RN91 sample peaks at $[\text{Fe}/\text{H}] \approx -1.6$, in agreement with recent results for the inner halo population (Carollo et al. 2007, 2010). On the contrary, the metallicity distribution related to the H V sample appears to be bimodal with an absolute maximum at $[\text{Fe}/\text{H}] \approx -2.2$ and a relative maximum at $[\text{Fe}/\text{H}] \approx -1.0$. The bimodality is probably an artefact due to selection effects and/or disk contamination for the following reasons²: (i) the H V sample is mainly made of inner halo stars (H V); (ii) the expected peak at $[\text{Fe}/\text{H}] \approx -1.6$ (Carollo et al. 2007, 2010) is lacking; (iii) the metallicity distribution from the RN91 sample can be scaled to match its counterpart from the H V sample within the range, $-3.4 < [\text{Fe}/\text{H}] < -2.6$ (H V); (iv) a bimodal metallicity distribution cannot be fitted to its theoretical counterpart deduced from simple models of chemical evolution, even if the latter is “observed” by applying the metal-poor selection criteria used in the Hamburg/ESO survey (H V).

The H V sample is mainly made of giant stars. A subsequent study on the stellar content of the Hamburg/ESO survey has been focused on a sample ($N = 617$) of main sequence turnoff stars (Li et al. 2010). Both samples exhibit a quite analogous metal abundance distribution where the halo population dominates ($[\text{Fe}/\text{H}] < -2.0$), while the contrary holds for higher values ($[\text{Fe}/\text{H}] > -2.0$). In the latter case, the H V sample is also affected from the survey-volume effect. For further details refer to the parent paper (Li et al. 2010).

Basing on the above considerations, the following working hypotheses are made.

- (1) The H V sample ($N = 3439$) is representative of the inner halo within the range, $-4.2 < [\text{Fe}/\text{H}] < -2.8$, where selection effects are minimized and contamination from disk stars is negligible (H V).
- (2) The RN91 sample ($N = 372$) is representative of the inner halo within the range, $-3.0 < [\text{Fe}/\text{H}] < +0.2$, with a caveat due to contamination from disk stars for $[\text{Fe}/\text{H}] > -1.0$ (RN91).
- (3) The RN91 and H V sample are equally representative (even if belonging

²The problem was raised via e-mail (December 2009) to two coauthors of the parent paper (H V) and to two coauthors of the paper where inner and outer halo populations were first detected (Carollo et al. 2007), but no reply was received up to-day. It cannot be excluded that related messages have been lost into the spam bin.

to different populations) of the inner halo within the range, $-3.0 \leq [\text{Fe}/\text{H}] \leq -2.8$, where the number of stars is $(\Delta N)_{\text{RN91}} = 8$ and $(\Delta N)_{\text{HV}} = 160$, respectively.

Accordingly, the fs10 sample can be built up from the RN91 and H V samples, by normalizing to the same number of stars within the metallicity range where the above mentioned samples are supposed to be equally representative of the inner halo. More specifically, the normalization shall be performed with respect to the H V sample, but the Poissonian error related to each bin shall remain unchanged with respect to the parent sample, with the minimum among the two retained for the bin where the parent samples are equally representative of the inner halo. Then the number of stars belonging to the fs10 sample, with regard to a selected metallicity bin, remains unchanged or is multiplied by a factor 20 according if the parent sample is H V ($[\text{Fe}/\text{H}] \leq -2.8$) or RN91 ($[\text{Fe}/\text{H}] > -2.8$), yielding a fictitious population, $N = 7452$.

2.2 The [O/H]-[Fe/H] empirical relation

In dealing with simple models of chemical evolution, involving the assumption of instantaneous recycling, the predicted metal abundance has to be compared to the observed oxygen (or any other primary element) abundance (e.g., Pagel 1989; C00; C01). Unfortunately, oxygen is more difficult than iron to detect, and an empirical formula may be needed to express the former as a function of the latter. The population of available samples where oxygen abundances are directly determined, does not exceed a few hundreds at most (e.g., Ramirez et al. 2007; Melendez et al. 2008; RB09; Fal09; Sal09). With regard to the halo, only the RB09 and Fal09 samples can be considered as representative, while the Sal09 sample shall be included for comparison, and the remaining above quoted two shall be excluded.

The RB09 sample ($N = 49$) is made of a homogeneous subsample ($N = 24$) of metal-poor ($-3.5 < [\text{Fe}/\text{H}] < -2.2$) stars, and a non homogeneous subsample ($N = 25$) of higher-metallicity ($-3.1 < [\text{Fe}/\text{H}] < -0.5$) stars. In both cases, the stellar population remains unspecified and oxygen abundance has been determined using standard local thermodynamical equilibrium (LTE) one-dimensional hydrostatic model atmospheres. The calculated oxygen abundance is independent of the solar value. Typical uncertainties are $\Delta[\text{Fe}/\text{H}] = \mp 0.15$ and $\Delta[\text{O}/\text{H}] = \mp 0.15$. Standard deviations are also provided for each star. For further details refer to the parent paper (RB09).

The Fal09 sample ($N = 43$) is made of halo stars ($-3.3 < [\text{Fe}/\text{H}] < -1.0$) where oxygen abundance has been determined using three different methods involving (a) LTE one-dimensional hydrostatic model atmospheres; (b)

Table 1: Values of effective temperature, T_{eff} , decimal logarithm of surface gravity, $\log g$, iron abundance, $[\text{Fe}/\text{H}]$, and oxygen abundance, $[\text{O}/\text{H}]$, for $N = 11$ stars in common between the RB09 and Fal09 sample. With regard to the latter, oxygen abundance has been determined using three different methods, LTE, SH0, SH1, respectively, and oxygen abundances related to LP831-070 are upper limits. For further details refer to the text.

star	RN09				Fal09					
	T_{eff}	$\log g$	$[\text{Fe}/\text{H}]$	$[\text{O}/\text{H}]$ LTE	T_{eff}	$\log g$	$[\text{Fe}/\text{H}]$	$[\text{O}/\text{H}]$ LTE	$[\text{O}/\text{H}]$ SH0	$[\text{O}/\text{H}]$ SH1
LP651-04	6030	4.26	-2.89	-2.04	6371	4.20	-2.63	-1.62	-2.21	-1.93
BD-13°3442	6090	4.11	-2.91	-2.15	6366	3.99	-2.69	-1.77	-2.39	-2.11
G11-44	5820	3.58	-2.29	-1.63	6178	4.35	-2.03	-1.29	-1.47	-1.40
G64-12	6074	3.72	-3.45	-2.24	6435	4.26	-3.24	-2.21	-3.10	-2.71
G64-37	6122	3.87	-3.28	-2.32	6432	4.24	-3.08	-2.24	-3.12	-2.70
LP635-14	5932	3.57	-2.71	-2.00	6367	4.11	-2.39	-1.60	-2.03	-1.85
LP815-43	6405	4.37	-2.76	-1.86	6483	4.21	-2.71	-1.95	-2.70	-2.36
HD084937	6206	3.89	-2.20	-1.49	6357	4.07	-2.11	-1.39	-1.64	-1.56
HD140283	5692	3.47	-2.56	-1.72	5849	3.72	-2.38	-1.67	-1.91	-1.81
HD194598	5875	4.20	-1.25	-1.00	6020	4.30	-1.15	-0.51	-0.75	-0.68
LP831-070	5985	4.75	-3.06	-2.45	6232	4.36	-2.93	-2.13	-2.95	-2.54

three-dimensional hydrostatic model atmospheres in absence of LTE with no account taken of the inelastic collisions via neutral H atoms ($S_{\text{H}} = 0$), hereafter quoted as SH0; (c) three-dimensional hydrostatic model atmospheres in absence of LTE with due account taken of the inelastic collisions via neutral H atoms ($S_{\text{H}} = 1$), hereafter quoted as SH1. For a single object (LP831-070) only an upper limit to oxygen abundance has been determined. Typical uncertainties are $\Delta[\text{Fe}/\text{H}] = \mp 0.15$ and $\Delta[\text{O}/\text{H}] = \mp 0.15$. Standard deviations are not provided for each star. For further details refer to the parent paper (Fal09).

The RB09 and Fal09 samples have $N = 11$ (necessarily halo) stars in common, where the values assumed for effective temperature and surface gravity have been determined using different methods, yielding different values for each star, as shown in Table 1. A comparison between $[\text{O}/\text{H}]-[\text{Fe}/\text{H}]$ empirical relations deduced from the data listed in Table 1, in connection with RB09 and Fal09 (case LTE, left; SH1, right) samples, is presented in Fig. 1, upper panels, while the correspondance between $[\text{Fe}/\text{H}]$ (left) and $[\text{O}/\text{H}]$ (right),

deduced from the above mentioned data, is shown in lower panels. With regard to Fal09 sample, case SH0 has not been considered, as it seems to overcorrect LTE abundances and yield values of $[\text{O}/\text{Fe}]$ which are probably too low. For further details refer to the parent paper (Fal09).

It can be seen that the $[\text{O}/\text{H}]-[\text{Fe}/\text{H}]$ empirical relation is slightly affected by the parent sample in the LTE case, with the exception of the most metal-rich sample object (Fig. 1, top left panel). A low discrepancy appears in the SH1 case (Fig. 1, top right panel), where results in absence of LTE approximation are available for the Fal09 sample only. The occurrence of a systematic difference in $[\text{Fe}/\text{H}]$ determinations is probably due to different methods related to different samples, which makes all points lie above the straight line with unit slope (Fig. 1, bottom left panel). The same holds, though to a lesser extent, for $[\text{O}/\text{H}]$ determinations related to LTE case (Fig. 1, bottom right panel, squares), while points related to the SH1 case (Fig. 1, bottom right panel, crosses) lie both above and below the straight line with unit slope.

The normalized $[\text{Fe}/\text{H}]$ distributions related to the RB09 and Fal09 sample are plotted in Fig. 2 (upper panels), where a similar trend is shown and, in particular, both exhibit a peak near $[\text{Fe}/\text{H}] = -2.2$, similar to their counterpart deduced from the HV sample (bottom right panel) but in contrast with their counterpart deduced from the RN91 sample (bottom left panel). Then the RB09 and Fal09 samples seem to be more representative of the outer halo than the inner halo, where the most populated metallicity bin is placed at $[\text{Fe}/\text{H}] \approx -2.2$ and $[\text{Fe}/\text{H}] \approx -1.6$, respectively (Carollo et al. 2007, 2010). Accordingly, the determination of the EDOD from the $[\text{Fe}/\text{H}]$ distribution related to RN91 and HV samples has to be made under the assumption that the $[\text{O}/\text{H}]-[\text{Fe}/\text{H}]$ empirical relations, deduced from the RB09 and Fal09 samples, hold to a similar extent for both the inner and the outer halo.

The following regression models are used for fitting to $[\text{O}/\text{H}]-[\text{Fe}/\text{H}]$ empirical relations.

- G** heteroscedastic functional models where the errors in X and in Y are uncorrelated (York 1966).
- Y** homoscedastic structural models where the errors in X are negligible (ideally null) with respect to the errors in Y (Isobe et al. 1990, OLS(Y|X) therein³).

³The captions, OLS(Y|X) and OLS(X|Y), have to be interchanged one with the other in Table 1 of the quoted paper.

- X** homoscedastic structural models where the errors in Y are negligible (ideally null) with respect to the errors in X (Isobe et al. 1990, OLS(X|Y) therein⁴).
- B** homoscedastic structural models where the regression line bisects the angle formed by the regression lines related to models Y and X above (Isobe et al. 1990, OLS bisector therein).
- O** homoscedastic structural or functional models where the regression line minimizes the sum of the perpendicular distances between the data points and the line (Isobe et al. 1990; Feigelson and Babu 1992; orthogonal regression therein).
- R** homoscedastic structural models where the regression line has slope equal to the geometric mean of the slopes of the regression lines related to models Y and X above (Isobe et al. 1990, reduced major-axis therein).

The [O/H]-[Fe/H] empirical relations deduced from RB09, Fal09 (cases LTE, SH0, SH1), and Sal09 samples, shown in Fig. 3, are interpolated using the regression models listed above. For heteroscedastic data and homoscedastic models, the typical uncertainties are assigned to all the data points. The results are listed in Table 2. An inspection of Fig. 3 and Table 2 shows that systematic errors related to different methods and/or different spectral lines in oxygen abundance determination, are dominant on both the dispersion due to measurement errors and intrinsic scatter. At this stage, a precise fit to the data extracted from a selected sample would be meaningless, and only acceptable fits related to different situations shall be considered. Accordingly, the following [O/H]-[Fe/H] empirical relations:

$$[\text{O}/\text{H}] = 0.72[\text{Fe}/\text{H}] \quad ; \quad (1)$$

with regard to the RB09 sample, Fig. 3 (full lines on data points), and

$$[\text{O}/\text{H}] = [\text{Fe}/\text{H}] + 0.70 \quad ; \quad (2)$$

with regard to the Fal09 sample, case SH1, Fig. 3 (dashed lines on data points), shall be used for determining the EDOD from the [Fe/H] distribution, related to a selected sample. The regression lines related to five different methods listed in Table 2, are shown for each sample on the top right panel of Fig. 3.

⁴The captions, OLS(X|Y) and OLS(Y|X), have to be interchanged one with the other in Table 1 of the quoted paper.

Table 2: Regression line slope and intercept estimators, \hat{a} and \hat{b} , and related dispersion estimators, $\hat{\sigma}_{\hat{a}}$, and $\hat{\sigma}_{\hat{b}}$, for the models (m) mentioned in the text, applied to the [O/H]-[Fe/H] empirical relation deduced from the following samples: RB09 (top left); Fal09, cases LTE (top right), SH0 (middle right), SH1 (bottom right); and Sal09 (middle left).

m	\hat{a}	$\hat{\sigma}_{\hat{a}}$	\hat{b}	$\hat{\sigma}_{\hat{b}}$	\hat{a}	$\hat{\sigma}_{\hat{a}}$	\hat{b}	$\hat{\sigma}_{\hat{b}}$
G	0.7279	0.0294	+0.0043	0.0672	0.9150	0.0305	0.5877	0.0666
Y	0.6917	0.0268	-0.0766	0.0598	0.8961	0.0333	0.5476	0.0761
X	0.7600	0.0326	+0.0742	0.0811	0.9381	0.0294	0.6366	0.0665
B	0.7253	0.0278	-0.0025	0.0665	0.9169	0.0310	0.5916	0.0706
O	0.7143	0.0282	-0.0268	0.0658	0.9150	0.0319	0.5877	0.0725
R	0.7251	0.0278	-0.0030	0.0664	0.9168	0.0310	0.5916	0.0706
G	0.6383	0.0435	+0.0619	0.0251	1.2640	0.0436	0.9519	0.0953
Y	0.5868	0.0596	+0.0908	0.0211	1.2261	0.0459	0.8717	0.1017
X	0.8077	0.0563	+0.2011	0.0422	1.2884	0.0434	1.0037	0.1003
B	0.6916	0.0513	+0.1431	0.0282	1.2568	0.0441	0.9367	0.0998
O	0.6476	0.0620	+0.1212	0.0268	1.2640	0.0449	0.9519	0.1019
R	0.6885	0.0523	+0.1416	0.0279	1.2569	0.0441	0.9369	0.0998
G					1.0732	0.0343	0.7027	0.0750
Y					1.0492	0.0358	0.6518	0.0808
X					1.0946	0.0315	0.7479	0.0730
B					1.0716	0.0332	0.6993	0.0760
O					1.0732	0.0337	0.7027	0.0772
R					1.0716	0.0332	0.6993	0.0760

2.3 The empirical differential oxygen abundance distribution (EDOD)

With regard to a selected $[\text{O}/\text{H}]$ - $[\text{Fe}/\text{H}]$ empirical relation:

$$[\text{O}/\text{H}] = a[\text{Fe}/\text{H}] + b \quad ; \quad (3)$$

and a specified $[\text{Fe}/\text{H}]$ distribution, let $[\text{Fe}/\text{H}]$, $[\text{Fe}/\text{H}]^\mp$, be the coordinates of a selected bin centre and bin left $(-)$ and right $(+)$ extremum, respectively, and $[\text{O}/\text{H}]$, $[\text{O}/\text{H}]^\mp$ their counterparts deduced via Eq. (3) for the related $[\text{O}/\text{H}]$ distribution. Accordingly, the bin semiamplitude reads:

$$\Delta^\mp[\text{O}/\text{H}] = \frac{[\text{O}/\text{H}]^+ - [\text{O}/\text{H}]^-}{2} = a \frac{[\text{Fe}/\text{H}]^+ - [\text{Fe}/\text{H}]^-}{2} = a\Delta^\mp[\text{Fe}/\text{H}] \quad ; \quad (4)$$

where $[\text{Fe}/\text{H}]$ and $[\text{O}/\text{H}]$ are logarithmic number abundances normalized to the solar value (e.g., C07).

The oxygen mass abundance normalized to the solar value, ϕ , to a good extent may be expressed as (e.g., C07):

$$\phi = \frac{Z_{\text{O}}}{(Z_{\text{O}})_{\odot}} = \exp_{10} [\text{O}/\text{H}] \quad ; \quad (5)$$

and a selected bin centre and bin semiamplitude, related to the $[\text{O}/\text{H}]$ distribution, read (e.g., C07):

$$\phi = \frac{1}{2} \{ \exp_{10} [\text{O}/\text{H}]^+ + \exp_{10} [\text{O}/\text{H}]^- \} \quad ; \quad (6)$$

$$\Delta^\mp \phi = \frac{1}{2} \{ \exp_{10} [\text{O}/\text{H}]^+ - \exp_{10} [\text{O}/\text{H}]^- \} \quad ; \quad (7)$$

where the bin width is variable for a constant bin width related to the $[\text{O}/\text{H}]$ distribution. The $[\text{O}/\text{H}]$ - $[\text{Fe}/\text{H}]$ and ϕ - $[\text{Fe}/\text{H}]$ empirical relations, expressed by Eqs. (1) and (2), by use of Eqs. (6) and (7) in the latter case, are represented in Table 3, where $B_{\text{F}} = [\text{Fe}/\text{H}]$ and $B_{\text{O}} = [\text{O}/\text{H}]$ to save space.

Following recent attempts (Rocha-Pinto and Maciel 1996; C00; C01; C07), the EDOD in a selected class of objects is defined as:

$$\psi(\phi) = \log \frac{\Delta N}{N \Delta \phi} \quad ; \quad (8)$$

where ΔN is the number of objects within a normalized oxygen abundance bin, $\Delta \phi$, centered in ϕ , and N is the number of sample objects. The increment

Table 3: The normalized oxygen abundance, $\phi = Z_{\text{O}}/(Z_{\text{O}})_{\odot}$, for two different [O/H]-[Fe/H] empirical relations deduced from interpolation to two different data sets, namely RB09 in presence of the local thermodynamic equilibrium approximation (left side), and Fal09 in absence of the local thermodynamic equilibrium approximation, case SH1 (right side). Upper and lower values for each bin are denoted by the apex + and -, respectively. The corresponding bin mean value and semiamplitude, with regard to normalized oxygen abundance, are labelled as ϕ and $\Delta^{\mp}\phi$, respectively. Labels B_{F}^{\mp} and B_{O}^{\mp} stand for [Fe/H] $^{\mp}$ and [O/H] $^{\mp}$, respectively.

		[O/H] = 0.72 [Fe/H] (RB09)				[O/H] = [Fe/H] + 0.70 (Fal09)			
B_{F}^{-}	B_{F}^{+}	B_{O}^{-}	B_{O}^{+}	ϕ	$\Delta^{\mp}\phi$	B_{O}^{-}	B_{O}^{+}	ϕ	$\Delta^{\mp}\phi$
-4.2	-4.0	-3.024	-2.880	1.1322D-3	1.8601D-4	-3.5	-3.3	4.0871D-4	9.2480D-4
-4.0	-3.8	-2.880	-2.736	1.5774D-3	2.5914D-4	-3.3	-3.1	6.4776D-4	1.4657D-3
-3.8	-3.6	-2.736	-2.592	2.1976D-3	3.6102D-4	-3.1	-2.9	1.0266D-3	2.3230D-3
-3.6	-3.4	-2.592	-2.448	3.0615D-3	5.0296D-4	-2.9	-2.7	1.6271D-3	3.6817D-3
-3.4	-3.2	-2.448	-2.304	4.2652D-3	7.0071D-4	-2.7	-2.5	2.5788D-3	5.8351D-3
-3.2	-3.0	-2.304	-2.160	5.9421D-3	9.7619D-4	-2.5	-2.3	4.0871D-3	9.2480D-3
-3.0	-2.8	-2.160	-2.016	8.2783D-3	1.3600D-3	-2.3	-2.1	6.4776D-3	1.4657D-2
-2.8	-2.6	-2.016	-1.872	1.1533D-2	1.8947D-3	-2.1	-1.9	1.0266D-2	2.3230D-2
-2.6	-2.4	-1.872	-1.728	1.6067D-2	2.6396D-3	-1.9	-1.7	1.6271D-2	3.6817D-2
-2.4	-2.2	-1.728	-1.584	2.2384D-2	3.6774D-3	-1.7	-1.5	2.5788D-2	5.8351D-2
-2.2	-2.0	-1.584	-1.440	3.1185D-2	5.1231D-3	-1.5	-1.3	4.0871D-2	9.2480D-2
-2.0	-1.8	-1.440	-1.296	4.3445D-2	7.1373D-3	-1.3	-1.1	6.4776D-2	1.4657D-1
-1.8	-1.6	-1.296	-1.152	6.0526D-2	9.9434D-3	-1.1	-0.9	1.0266D-1	2.3230D-1
-1.6	-1.4	-1.152	-1.008	8.4322D-2	1.3853D-2	-0.9	-0.7	1.6271D-1	3.6817D-1
-1.4	-1.2	-1.008	-0.864	1.1747D-1	1.9299D-2	-0.7	-0.5	2.5788D-1	5.8351D-1
-1.2	-1.0	-0.864	-0.720	1.6366D-1	2.6887D-2	-0.5	-0.3	4.0871D-1	9.2480D-1
-1.0	-0.8	-0.720	-0.576	2.2800D-1	3.7457D-2	-0.3	-0.1	6.4776D-1	1.4657D-1
-0.8	-0.6	-0.576	-0.432	3.1764D-1	5.2184D-2	-0.1	+0.1	1.0266D+0	2.3230D-1
-0.6	-0.4	-0.432	-0.288	4.4253D-1	7.2700D-2	+0.1	+0.3	1.6271D+0	3.6817D-1
-0.4	-0.2	-0.288	-0.144	6.1651D-1	1.0128D-1	+0.3	+0.5	2.5788D+0	5.8351D-1
-0.2	+0.0	-0.144	+0.000	8.5890D-1	1.4110D-1	+0.5	+0.7	4.0871D+0	9.2480D-1
+0.0	+0.2	+0.000	+0.144	1.1966D-0	1.9658D-1	+0.7	+0.9	6.4776D+0	1.4657D-1
+0.2	+0.4	+0.144	+0.288	1.6670D-0	2.7386D-1	+0.9	+1.1	1.0266D+1	2.3230D-1

ratio, $\Delta N/\Delta\phi$, used in earlier attempts (Pagel 1989; Malinie et al. 1993) is replaced by its normalized counterpart, $\Delta N/(N\Delta\phi)$, to allow comparison between different samples. The uncertainty on ΔN is evaluated from Poisson errors (e.g., RN91), as $\sigma_{\Delta N} = (\Delta N)^{1/2}$, and the related uncertainty in the EDOD is:

$$\Delta^\mp\psi = |\psi - \psi^\mp| = \log \left[1 \mp \frac{(\Delta N)^{1/2}}{\Delta N} \right] ; \quad (9a)$$

$$\psi^\mp = \log \frac{\Delta N \mp (\Delta N)^{1/2}}{N\Delta\phi} ; \quad (9b)$$

where $\psi^- \rightarrow -\infty$ in the limit $\Delta N \rightarrow 1$. For further details refer to the parent papers (C01; C07).

The EDOD related to RN91, HV, and fs10 samples are listed in Table 4 for the [O/H]-[Fe/H] empirical relations expressed by Eqs. (1) and (2), left and right side, respectively. The EDOD related to the fs10 sample, taken to be representative of the inner halo, is plotted in Fig. 4 for the [O/H]-[Fe/H] empirical relations expressed by Eqs. (1) and (2), left and right panel, respectively. Upper panels represent the whole distribution, while lower panels zoom the low-metallicity range. The vertical bars on the horizontal axis mark $[\text{Fe}/\text{H}] = -2.2$, -1.6 , where the global $[\text{Fe}/\text{H}]$ distribution of the outer and inner halo, respectively, peak according to recent results (Carollo et al. 2007, 2010), and $[\text{Fe}/\text{H}] = -0.8$, where a transition from halo to bulge/disk globular clusters occurs (Mackey and van den Bergh 2005).

A main feature of the EDODs plotted in Fig. 4, is the presence of five regions characterized by a nearly linear trend, which shall be named O, A, F, C, E, respectively, and defined in the following metallicity ranges, each containing n_X bins, $X=O, A, F, C, E$.

- O** $[\text{Fe}/\text{H}] < -4.2$; $[\text{Fe}/\text{H}] > -0.2$; $n_O \rightarrow +\infty$; the distribution coincides with the horizontal axis after removing a single high-metallicity star from the RN91 sample, considered as due to disk contamination or, in any case, an outlier. On the other hand, the last appears in related tables and figures for comparison.
- A** $-4.2 \leq [\text{Fe}/\text{H}] \leq -2.7$; $n_A = 6$; the distribution is steep with positive slope.
- F** $-2.7 \leq [\text{Fe}/\text{H}] \leq -1.7$; $n_F = 6$; the distribution is mild with negative slope.
- C** $-1.7 \leq [\text{Fe}/\text{H}] \leq -0.9$; $n_C = 5$; the distribution is steep with negative slope.

Table 4: The empirical, differential oxygen abundance distribution (EDOD) in the inner halo, deduced from the fs10 sample ($N = 7452$) using two different $[\text{O}/\text{H}]-[\text{Fe}/\text{H}]$ empirical relations, determined from interpolation to two different data sets, RB09 in presence of the local thermodynamic equilibrium approximation (left side), and Fal09 in absence of the local thermodynamic equilibrium approximation, case SH1 (right side). The fictitious fs10 sample results from the combination of the H V sample ($N = 3439$) for lower metallicities, $-4.2 \leq [\text{Fe}/\text{H}] < -3.0$, and the RN91 sample ($N = 372$) for higher metallicities, $-2.8 < [\text{Fe}/\text{H}] \leq +0.2$, under the assumption that the two samples are equally representative of the inner halo within the metallicity bin, $-3.0 \leq [\text{Fe}/\text{H}] \leq -2.8$. The error on the generic bin height has been estimated from the Poissonian error of its counterpart related to the parent sample. See text for further details.

$[\text{O}/\text{H}] = 0.72 [\text{Fe}/\text{H}]$ (RB09)				$[\text{O}/\text{H}] = [\text{Fe}/\text{H}] + 0.70$ (Fal09)		
ϕ	ψ	$\Delta^- \psi$	$\Delta^+ \psi$	ϕ	ψ	$\Delta^- \psi$
1.1322D-3	-1.4181D-1	5.3329D-1	2.3226D-1	4.0871D-4	+1.6168D-1	5.3329D-1
1.5774D-3				6.4776D-4		
2.1976D-3				1.0266D-3		
3.0615D-3	+2.0434D-1	1.4793D-1	1.1014D-1	1.6271D-3	+3.3983D-1	1.4793D-1
4.2652D-3	+6.3437D-1	4.7712D-1	2.2185D-1	2.5788D-3	+7.1386D-1	4.7712D-1
5.9421D-3	+7.0048D-1	3.2187D-1	1.8282D-1	4.0871D-3	+7.2397D-1	3.2187D-1
8.2783D-3	+8.9728D-1	1.8947D-1	1.3148D-1	6.4776D-3	+8.6477D-1	1.8947D-1
1.1533D-2	+9.6413D-1	1.4107D-1	1.0631D-1	1.0266D-2	+8.7562D-1	1.4107D-1
1.6067D-2	+1.0284D-0	1.0691D-1	8.5725D-2	1.6271D-2	+8.8390D-1	1.0691D-1
2.2384D-2	+9.4240D-1	9.9155D-2	8.0671D-2	2.5788D-2	+7.4189D-1	9.9155D-2
3.1185D-2	+9.4967D-1	8.1707D-2	6.8742D-2	4.0871D-2	+6.9316D-1	8.1707D-2
4.3445D-2	+9.1764D-1	7.0967D-2	6.0983D-2	6.4776D-2	+6.0513D-1	7.0967D-2
6.0526D-2	+9.2258D-1	5.8986D-2	5.1924D-2	1.0266D-1	+5.5407D-1	5.8986D-2
8.4322D-2	+6.9376D-1	6.5516D-2	5.6916D-2	1.6271D-1	+2.6925D-1	6.5516D-2
1.1747D-1	+4.7566D-1	7.1860D-2	6.1640D-2	2.5788D-1	-4.8510D-3	7.1860D-2
1.6366D-1	+1.4535D-1	9.0970D-2	7.5175D-2	4.0871D-1	-3.9116D-1	9.0970D-2
2.2800D-1	-3.3187D-1	1.4107D-1	1.0631D-1	6.4776D-1	-9.2438D-1	1.4107D-1
3.1764D-1	-5.1063D-1	1.4793D-1	1.1014D-1	1.0266D+0	-1.1591D-0	1.4793D-1
4.4253D-1	-8.8871D-1	2.0618D-1	1.3924D-1	1.6271D+0	-1.5932D-0	2.0618D-1
6.1651D-1	-1.1788D-0	2.5744D-1	1.6053D-1	2.5788D+0	-1.9393D-0	2.5744D-1
8.5890D-1				4.0871D+0		
1.1966D-0	-2.1658D+0	$+\infty$	3.0103D-1	6.4776D+0	-3.0383D-0	$+\infty$
1.6670D-0				1.0266D+1		

E $-0.9 \leq [\text{Fe}/\text{H}] \leq -0.2$; $n_{\text{E}} = 4$; the distribution is less steep with negative slope.

In absence of LTE approximation with regard to the $[\text{O}/\text{H}]-[\text{Fe}/\text{H}]$ empirical relation deduced from the Fal09 sample (case SH1), regions F and C may merge into a single region, FC, within the range, $-2.7 \leq [\text{Fe}/\text{H}] \leq -0.9$, including $n_{\text{FC}} = 10$ bins. The vertical dashed lines in Fig. 4 mark $[\text{Fe}/\text{H}] = -2.7, -1.7, -0.8$, from the left to the right. It can be seen that the global $[\text{Fe}/\text{H}]$ distribution peaks early within the F and C region for the outer and inner halo, respectively. In addition, data points on the boundary between adjacent regions follow the linear trend exhibited by every of them.

The regression line related to the EDOD within each populated region, has been determined using the B model listed in Table 2, under the assumption that the intrinsic scatter is dominant (Isobe et al. 1990). A single high-metallicity star from the RN91 sample, considered as due to disk contamination or, in any case, an outlier, has not been included in the fitting procedure. The regression line slope and intercept estimators and related dispersion estimators are listed in Table 5 for each region of the EDODs plotted in Fig. 4. The results are consistent (within $\mp\sigma$) with their counterparts determined using the other models listed in Table 2. The selection of a special method is of little relevance, due to the paucity of data within each region.

The regression lines are represented in Fig. 5 for each region (from the left to the right): A (dotted, positive slope), F (dotted, negative slope), C (full), E (dashed), with regard to the EDOD plotted in Fig. 4. In absence of LTE approximation, case SH1 (right panels), a more inclined dashed line fits to the FC region, in alternative to F and C regions separately. To ensure continuity, the above mentioned regions must be redefined by the intersections of regression lines, which make the transition from a selected region to the adjacent one. The results are listed in Table 6 for the EDOD and related regression lines plotted in Fig. 5. A vertical line instead of a regression line has been considered for the O region, where no data exist.

In conclusion, the EDOD related to the inner halo may be approximated, to a satisfactory extent, as the sum of four (A, F, C, E) or three (A, FC, E) regions, within which the trend is linear. An interpretation in terms of simple models of chemical evolution is highly attractive, as the corresponding TDOD shows, in fact, a linear trend (Pagel 1989; Rocha-Pinto and Maciel 1996; C00; C01; C07).

Table 5: Regression line slope and intercept estimators, \hat{a}_B and \hat{b}_B , and related dispersion estimators, $\hat{\sigma}_{\hat{a}_B}$, and $\hat{\sigma}_{\hat{b}_B}$, for the B model applied to the oxygen abundance distribution (EDOD) plotted in Fig. 4 with regard to different $[\text{O}/\text{H}]-[\text{Fe}/\text{H}]$ empirical relations, deduced from the RB09 sample in presence of LTE approximation via Eq. (1) (top panel), and from the Fal09 sample in absence of LTE approximation, case SH1, via Eq. (2) (bottom panel). The method has been applied to each region (X) separately. Data points on the boundary between adjacent regions are used for determining regression lines within both of them.

X	\hat{a}_B	$\hat{\sigma}_{\hat{a}_B}$	\hat{b}_B	$\hat{\sigma}_{\hat{b}_B}$
A	+1.1382 E+2	2.0648 E+1	-1.0567 E-1	1.2296 E-1
F	-2.0950 E+0	7.2725 E-1	+1.0188 E+0	2.9109 E-2
C	-7.3565 E+0	1.2375 E-1	+1.3433 E+0	2.3577 E-2
E	-2.2569 E+0	1.0098 E-1	+1.7784 E-1	3.2148 E-2
A	+7.9432 E+1	1.9364 E+1	+2.7571 E-1	9.2608 E-2
F	-3.8855 E+0	6.1570 E-1	+8.9453 E-1	2.9691 E-2
C	-2.6460 E+0	1.4542 E-1	+7.3661 E-1	5.9411 E-2
FC	-2.8643 E+0	1.3796 E-1	+8.2804 E-1	2.7988 E-2
E	-5.3661 E-1	3.5681 E-2	-6.1514 E-1	4.3965 E-2

Table 6: Transition points between adjacent regions, as determined from the intersection of related regression lines, for the oxygen abundance distribution (EDOD) plotted in Fig. 4 with regard to different $[\text{O}/\text{H}]-[\text{Fe}/\text{H}]$ empirical relations, deduced from the RB09 sample in presence of LTE approximation via Eq. (1) (left panel) and from the Fal09 sample in absence of LTE approximation, case SH1, via Eq. (2) (right panel). In the latter case, the FC region has also been considered in alternative to F and C regions separately. For further details refer to the text.

	RB09		Fal09 (SH1)	
transition	ϕ	ψ	ϕ	ψ
O-A	9.4624 E−4	+2.0383 E−3	3.1623 E−4	+3.0083 E−1
A-F	9.7001 E−3	+9.9844 E−1	7.4271 E−3	+8.6567 E−1
F-C	6.1687 E−2	+8.8953 E−1	1.2740 E−1	+9.9952 E−1
C-E	2.2854 E−1	−3.3795 E−1	6.4083 E−1	−9.5902 E−1
E-O	7.1779 E−1	−1.4421 E−0	3.1623 E−0	−2.3121 E−0
A-FC			6.7114 E−3	+8.0882 E−1
FC-E			6.2002 E−1	−9.4785 E−1

3 The model

In their original formulation, simple models of chemical evolution are closed-box (CB) i.e. mass conservation (gas + stars) holds (e.g., Searle and Sargent 1972; Pagel and Patchett 1975). In later formulation, a “reservoir” is added to the “box”, where mass conservation no longer occurs within the box, but still holds within the system box + reservoir. Accordingly, related models can be conceived as closed-(box+reservoir) (CBR) models. The gas within the box is “active” in the sense that allows star formation according to a specified birth-rate stellar function. The gas within the reservoir is “inhibited” in the sense that no star formation takes place. Gas may outflow from the box into the reservoir (H76) or inflow into the box from the reservoir (C07). The related TDOD is a straight line where the slope (to the knowledge of the author) is negative in all cases studied in literature (e.g., Pagel 1989; Rocha-Pinto and Maciel 1996; C00; C01; C07).

For this reason, the formulation of CBR models shall be extended to a TDOD with positive slope, under the standard assumptions of CB models: (i) instantaneous recycling within the box, where stars are divided into two categories, namely (a) short-lived, which instantaneously evolve, and (b)

long-lived, all of which are still evolving; (ii) instantaneous mixing within the box, where the gas returned from short-lived stars is instantaneously mixed with the interstellar medium yielding uniform composition; and the standard assumptions of CBR models: (iii) mass conservation within the system (box+reservoir); (iv) gas outflow from the box into the reservoir or inflow into the box from the reservoir, at a rate proportional to the star formation rate; (v) inhibition of star formation within the reservoir; (vi) gas outflow or inflow with same composition with respect to preexisting gas.

In this picture, the oxygen (or any other primary element) mass fraction can be determined, extending the procedure followed for CB models (e.g., Pagel and Patchett 1975; Wang and Silk 1993; C00) to CBR models.

3.1 Basic theory

The change in oxygen (or any other primary element) gas mass, M_{gO} , is owing to four contributions, as:

$$\frac{dM_{\text{gO}}}{dt} = \left(\frac{dM_{\text{gO}}}{dt} \right)_{\text{sf}} + \left(\frac{dM_{\text{gO}}}{dt} \right)_{\text{gr}} + \left(\frac{dM_{\text{gO}}}{dt} \right)_{\text{sdu}} + \left(\frac{dM_{\text{gO}}}{dt} \right)_{\text{sds}} ; \quad (10)$$

related to subtraction via star formation (sf), subtraction via outflow from the box into the reservoir or addition via inflow into the box from the reservoir (gr), addition via unsynthesised gas from short-lived stars (sdu), and addition via newly synthesised gas from short-lived stars (sds), respectively.

For simple CBR models, the following relations hold:

$$\frac{dM_{\text{g}}}{dt} = -\alpha \frac{dM_{\text{S}}}{dt} - \kappa \alpha \frac{dM_{\text{S}}}{dt} = -\alpha(1 + \kappa) \frac{dM_{\text{S}}}{dt} ; \quad (11)$$

$$\left(\frac{dM_{\text{gO}}}{dt} \right)_{\text{sf}} + \left(\frac{dM_{\text{gO}}}{dt} \right)_{\text{gr}} + \left(\frac{dM_{\text{gO}}}{dt} \right)_{\text{sdu}} = -Z_{\text{O}} \alpha (1 + \kappa) \frac{dM_{\text{S}}}{dt} ; \quad (12)$$

$$\left(\frac{dM_{\text{gO}}}{dt} \right)_{\text{sds}} = (1 - Z) \hat{p} \alpha \frac{dM_{\text{S}}}{dt} ; \quad (13)$$

where M_{g} is the mass in active gas, M_{S} is the global mass in gas which has been turned into stars, M_{gO} is the oxygen mass in active gas, α is the fraction in long-lived stars and stellar remnants within a star generation (lock parameter), κ is the ratio of flowing (outflow from the box into the reservoir or inflow into the box from the reservoir) gas rate to locking (in the form of long-lived stars and stellar remnants) gas rate (flow parameter), Z_{O} and Z are the oxygen and metal mass abundance, respectively, within the active gas, and \hat{p} is the ratio of the oxygen mass newly synthesised and returned

to the interstellar medium, for a metal-free initial composition⁵, to the mass locked up in long-lived stars and stellar remnants (yield parameter). The lock parameter, α , the flow parameter, κ , and the yield parameter, \hat{p} , for sake of brevity, in the following shall be quoted as the lock, the flow, and the yield, respectively.

The definition of oxygen mass abundance, Z_O , fractional active gas mass, μ , and fractional star mass, s , read:

$$Z_O = \frac{M_{gO}}{M_g} \quad ; \quad \mu = \frac{M_g}{M_0} \quad ; \quad s = \alpha S = \frac{\alpha M_S}{M_0} = \frac{M_s}{M_0} \quad ; \quad (14)$$

where $M_s = \alpha M_S$ is the mass in long-lived stars and stellar remnants, and M_0 is the total mass within the box at the starting configuration.

The substitution of Eqs. (11)-(13) into (10) yields:

$$\frac{dM_{gO}}{dt} = \left[Z_O - \frac{1-Z}{1+\kappa} \hat{p} \right] \frac{dM_g}{dt} \quad ; \quad (15)$$

and the fractional oxygen gas mass, via Eq. (14) reads:

$$\frac{M_{gO}}{M_0} = \frac{M_{gO}}{M_g} \frac{M_g}{M_0} = Z_O \mu \quad ; \quad (16)$$

where, in addition:

$$\frac{d(Z_O \mu)}{dt} = Z_O \frac{d\mu}{dt} + \mu \frac{dZ_O}{dt} \quad ; \quad (17)$$

on the other hand, in terms of fractional masses, Eq. (15) may be cast under the equivalent form:

$$\frac{d(Z_O \mu)}{dt} = \left[Z_O - \frac{1-Z}{1+\kappa} \hat{p} \right] \frac{d\mu}{dt} \quad ; \quad (18)$$

and the combination of Eqs. (17) and (18) yields:

$$\frac{dZ_O}{1-Z} = -\hat{p}'' \frac{d\mu}{\mu} \quad ; \quad (19)$$

$$\hat{p}'' = \frac{\hat{p}}{1+\kappa} \quad ; \quad (20)$$

where \hat{p}'' is the effective yield parameter, hereafter quoted as the effective yield (H76).

⁵This detail is usually omitted in literature.

In the special case of a linear Z_O - Z relation:

$$\frac{1 - Z_O}{1 - Z} = \frac{1}{A} \quad ; \quad A < 1 \quad ; \quad (21)$$

the combination of Eqs. (19) and (21) produces:

$$\frac{dZ_O}{1 - Z_O} = -A\hat{p}'' \frac{d\mu}{\mu} \quad ; \quad (22)$$

which can be integrated. After some algebra, the result is:

$$Z_O - (Z_O)_i = [1 - (Z_O)_i] \left[1 - \left(\frac{\mu}{\mu_i} \right)^{A\hat{p}''} \right] \quad ; \quad (23)$$

where the index, i , denotes the starting configuration at the cosmic time, t_i . Reversing the role of the variables, Eq. (23) reads:

$$\frac{\mu}{\mu_i} = \left[\frac{1 - Z_O}{1 - (Z_O)_i} \right]^{1/(A\hat{p}'')} \quad ; \quad (24)$$

which is monotonic in Z_O within the domain, $0 \leq Z_O \leq 1$.

Using the MacLaurin series development:

$$\left(\frac{\mu}{\mu_i} \right)^{A\hat{p}''} = \exp \left(A\hat{p}'' \ln \frac{\mu}{\mu_i} \right) = 1 + A\hat{p}'' \ln \frac{\mu}{\mu_i} + \dots \quad ; \quad (25)$$

under the further assumption that the terms of higher order with respect to the first can be neglected, Eq. (23) reduces to:

$$Z_O - (Z_O)_i = -[1 - (Z_O)_i] A\hat{p}'' \ln \frac{\mu}{\mu_i} \quad ; \quad (26)$$

$$\left| A\hat{p}'' \ln \frac{\mu}{\mu_i} \right| < \left| \hat{p}'' \ln \frac{\mu}{\mu_i} \right| < \left| \hat{p}'' \ln \frac{\mu_f}{\mu_i} \right| \ll 1 \quad ; \quad (27)$$

where the index, f , denotes the ending configuration at the cosmic time, t_f , and $\mu_i < \mu < \mu_f$ or $\mu_i > \mu > \mu_f$ owing to Eq. (24). The initial oxygen and metal abundance may safely be neglected with respect to unity, $(Z_O)_i \leq Z_i \ll 1$, which implies $A \rightarrow 1$ via Eq. (21). Accordingly, Eq. (26) reduces to:

$$Z_O - (Z_O)_i = -\hat{p}'' \ln \frac{\mu}{\mu_i} \quad ; \quad (28)$$

which is the classical formulation (H76).

It is worth emphasizing that the inequality, expressed by Eq. (27), does not affect the instantaneous recycling approximation, but only the general formulation expressed by Eq. (23) provided the $Z_{\text{O}}-Z$ relation is linear, according to Eq. (21). In general, it is assumed the instantaneous recycling approximation holds for sufficiently high fractional active gas mass fraction, $\mu \gtrsim 0.1$ (e.g., Prantzos 2007, Fig. 12 therein), but the threshold could be lowered using Eq. (23) instead of Eq. (26). In fact, neglecting the terms of higher order in the MacLaurin series, expressed by Eq. (25), makes oxygen abundance, Z_{O} , increased with respect to the general case, Eq. (23), which, in turn, is an upper limit with respect to the exact formulation, Eq. (19). More specifically, $\mu \rightarrow 0$ implies $Z_{\text{O}} \rightarrow 1$ according to Eq. (23) instead of $Z_{\text{O}} \rightarrow Z_{\text{O}}(\mu = 0) < 1$ due to the presence of other metals. Then the instantaneous recycling approximation expressed by Eq. (23), or better by the integral of Eq. (19), appears to hold well even below the threshold, $\mu \approx 0.1$.

In terms of fractional masses, Eq. (11) via Eq. (14) may be cast under the equivalent form:

$$\alpha(1 + \kappa) \frac{dS}{dt} = (1 + \kappa) \frac{ds}{dt} = -\frac{d\mu}{dt} ; \quad (29)$$

which can be read in the following way: any mass change in active gas is counterbalanced by a change in long-lived stars and stellar remnants plus a change in gas outflow from the box into the reservoir ($\kappa > 0$) or a change in gas inflow into the box from the reservoir ($\kappa < 0$). More specifically, a number of different flow regimes may be distinguished as listed below.

- Outflow regime ($\kappa > 0$), where star formation is inhibited (H76). For an exhaustive description refer to earlier attempts (C00; C01).
- Stagnation regime ($\kappa = 0$), where star formation is neither inhibited nor enhanced. Accordingly, CBR models reduce to CB models. For an exhaustive description refer to earlier attempts (Searle and Sargent 1972; Pagel and Patchett 1975).
- Moderate inflow regime ($-1 < \kappa < 0$), where star formation is enhanced and active gas mass fraction monotonically decreases in time. For an exhaustive description refer to an earlier attempt (C07).
- Steady inflow regime ($\kappa = -1$), where star formation is enhanced and active gas mass fraction remains unchanged.
- Strong inflow regime ($\kappa < -1$), where star formation is enhanced and active gas mass fraction monotonically increases in time.

The effective yield, \hat{p}'' , defined by Eq. (20), cannot exceed the real yield, \hat{p} , both in outflow and in strong inflow regime, while the contrary holds in moderate inflow regime and, *a fortiori*, in steady inflow regime, where a divergency occurs. For this reason, the effective yield cannot be considered alone, but together with the factor, $\ln[\mu/(\mu)_i]$. More specifically, the right-hand side of Eq. (28), $-\hat{p}'' \ln[\mu/(\mu)_i] = -\hat{p} \ln[\mu/(\mu)_i]/(1 + \kappa)$, is positive in all regimes due to the trend exhibited by the active gas mass fraction. In steady inflow regime, the following relation necessarily holds:

$$\lim_{\kappa \rightarrow -1} \left(\frac{-\hat{p}}{1 + \kappa} \ln \frac{\mu}{\mu_i} \right) = \frac{Z_O - (Z_O)_i}{(Z_O)_f - (Z_O)_i} = \frac{t - t_i}{t_f - t_i} ; \quad (30)$$

in terms of the oxygen abundance related to a constant active gas mass fraction, or in terms of the cosmic time.

In any case, mass conservation follows from integration of Eq. (29), as:

$$\mu + s + D = \mu_0 + s_0 + D_0 = \mu_0 = 1 ; \quad (31)$$

$$D = \alpha \kappa S = \kappa s ; \quad (32)$$

conformly to Eq. (14), where D is the gas mass fraction which outflowed from the box into the reservoir ($\kappa > 0$) or inflowed into the box from the reservoir ($\kappa < 0$). An equivalent form of Eq. (31) reads:

$$\mu + s = 1 - D ; \quad (33)$$

where variables on the left and the right-hand side member relate to the box and the reservoir, respectively.

The birth-rate stellar function (number of stars born per unit volume, mass, and time), needs to be specified for determining the temporal behaviour of gas and star fractional masses. Following an earlier attempt (C00), the selected choice reads:

$$\mathcal{B}(\tilde{m}, \tilde{t}) = \frac{B}{V} f(\mu) \Phi(\tilde{m}) ; \quad \tilde{m} = \frac{m}{m_\odot} ; \quad \tilde{t} = \frac{t}{\text{Gyr}} ; \quad (34)$$

where B is a normalization constant, V the volume of the box, $\Phi(\tilde{m})$ the stellar initial mass function and $f(\mu)$ an assigned function of the active gas mass fraction, which is the time-dependent term. The number of stars born per unit volume within an infinitesimal dimensionless mass range, $\tilde{m} \mp d\tilde{m}/2$, and infinitesimal dimensionless time range, $\tilde{t} \mp d\tilde{t}/2$, is $\mathcal{B}(\tilde{m}, \tilde{t}) d\tilde{m} d\tilde{t}$.

The number of long-lived stars generated (within the box) up to an assigned dimensionless cosmic time, \tilde{t} , is:

$$N_{\ell\ell}(\tilde{t}) = \int_{\tilde{t}_i}^{\tilde{t}} d\tilde{t} \int_{\tilde{m}_{\text{mf}}}^{\tilde{m}_{\ell\ell}} V \mathcal{B}(\tilde{m}, \tilde{t}) d\tilde{m} = B F(\tilde{t}) I'(5) ; \quad (35a)$$

$$F(\tilde{t}) = \int_{\tilde{t}_i}^{\tilde{t}} f(\mu) d\tilde{t} ; \quad I'(5) = \int_{\tilde{m}_{\text{mf}}}^{\tilde{m}_{\ell\ell}} \Phi(\tilde{m}) d\tilde{m} ; \quad (35b)$$

where m_{mf} is the lower stellar mass limit, and m_{ell} the upper mass limit of long-lived stars.

The mass fraction in stars globally generated (within the box) up to a dimensionless cosmic time, \tilde{t} , is:

$$S(\tilde{t}) = \int_{\tilde{t}_i}^{\tilde{t}} d\tilde{t} \int_{\tilde{m}_{\text{mf}}}^{\tilde{m}_{\text{Mf}}} \frac{V}{M_0} \mathcal{B}(\tilde{m}, \tilde{t}) d\tilde{m} = CF(\tilde{t}) ; \quad (36a)$$

$$C = \frac{Bm_{\odot}}{M_0} I(1) ; \quad I(1) = \int_{\tilde{m}_{\text{mf}}}^{\tilde{m}_{\text{Mf}}} \tilde{m} \Phi(\tilde{m}) d\tilde{m} ; \quad (36b)$$

where m_{Mf} is the upper stellar mass limit.

The mass fraction in long-lived stars and in gas outflowed from the box into the reservoir or inflowed into the box from the reservoir (in both cases with equal composition with respect to the preexisting gas), at an assigned dimensionless cosmic time, \tilde{t} , are:

$$s(\tilde{t}) = \alpha S(\tilde{t}) = \alpha CF(\tilde{t}) ; \quad (37)$$

$$D(\tilde{t}) = \alpha \kappa S(\tilde{t}) = \alpha \kappa CF(\tilde{t}) ; \quad (38)$$

according to the definition of lock and flow, respectively.

The star formation rate (within the box), the lock rate, and the flow rate at an assigned dimensionless cosmic time, \tilde{t} , are:

$$\frac{dS}{d\tilde{t}} = Cf(\mu) ; \quad (39)$$

$$\frac{ds}{d\tilde{t}} = \alpha Cf(\mu) ; \quad (40)$$

$$\frac{dD}{d\tilde{t}} = \alpha \kappa Cf(\mu) ; \quad (41)$$

and the combination of Eqs. (29) and (39) yields:

$$\alpha(1 + \kappa)Cf(\mu) = -\frac{d\mu}{d\tilde{t}} ; \quad (42)$$

which is equivalent to:

$$\int_{\mu_i}^{\mu} \frac{d\mu}{f(\mu)} = -\alpha(1 + \kappa)C(\tilde{t} - \tilde{t}_i) ; \quad (43)$$

in the special case, $f(\mu) = \mu$, Eq. (43) can be integrated as:

$$\mu = \mu_i \exp[-\alpha(1 + \kappa)C(\tilde{t} - \tilde{t}_i)] ; \quad (44)$$

and the combination of Eqs. (20), (28), and (44) yields a linear trend for the oxygen abundance:

$$Z_O - (Z_O)_i = \hat{p}\alpha C(\tilde{t} - \tilde{t}_i) \quad ; \quad (45)$$

regardless of the flow, κ .

In the more general case, $f(\mu) = \mu^\nu$, Eq. (39) reduces to a Schmidt (1959, 1963) star formation law. Leaving aside the above discussed special case, $\nu = 1$, Eq. (43) can be integrated and, after some algebra, the result is:

$$\mu = \mu_i \left[1 - \frac{1 - \nu}{\mu_i^{1-\nu}} \alpha(1 + \kappa) C(\tilde{t} - \tilde{t}_i) \right]^{1/(1-\nu)} \quad ; \quad \nu \neq 1 \quad ; \quad (46)$$

which, using the logarithm Taylor series, $\ln(1 + x) = x - x^2/2 + x^3/3 - \dots$, $|x| < 1$, and neglecting the terms of higher order with respect to the first, may be approximated as:

$$\mu = \mu_i \exp \left[-\mu_i^{\nu-1} \alpha(1 + \kappa) C(\tilde{t} - \tilde{t}_i) \right] \quad ; \quad (47a)$$

$$\left| (1 - \nu) \mu_i^{\nu-1} \alpha(1 + \kappa) C(\tilde{t} - \tilde{t}_i) \right| \ll 1 \quad ; \quad (47b)$$

in the limit, $\nu \rightarrow 1$, Eqs. (44) and (47a) coincide, as expected. The combination of Eqs. (20), (28), and (47) yields:

$$Z_O - (Z_O)_i = \hat{p} \mu_i^{\nu-1} \alpha C(\tilde{t} - \tilde{t}_i) \quad ; \quad (48)$$

regardless of the flow, κ . Then a Schmidt star formation law with exponent, $\nu \approx 1$, implies a linear dependence of the oxygen (or any other primary element) abundance on the cosmic time.

In general, simple CBR models are described by Eqs. (28) and (43), the latter only for including the temporal behaviour.

3.2 Theoretical differential oxygen abundance distribution (TDOD)

For a selected spectral class, the number of long-lived stars generated (within the box) up to an assigned dimensionless cosmic time, is:

$$N(\tilde{t}) = \int_{\tilde{t}_i}^{\tilde{t}} d\tilde{t} \int_{\tilde{m}_1}^{\tilde{m}_2} V \mathcal{B}(\tilde{m}, \tilde{t}) = C_{12} F(\tilde{t}) \quad ; \quad (49a)$$

$$C_{12} = B I'(1, 2) \quad ; \quad I'(1, 2) = \int_{\tilde{m}_1}^{\tilde{m}_2} \Phi(\tilde{m}) d\tilde{m} \quad ; \quad (49b)$$

where m_1 and m_2 are the lower and upper mass limit of the spectral class.

For simple CBR models, the oxygen abundance is monotonically increasing in time owing to Eqs. (23) and (46), which implies the number of stars born up to the cosmic time, t , coincides with the number of stars with oxygen abundance up to the related value, $Z_O(t)$, or $N(t) = N(Z_O)$. The same holds for the long-lived star mass fraction (including stellar remnants), $s(t) = s(Z_O)$. By use of Eq. (14), the long-lived star mass fraction and the number of long-lived stars, $N_{\ell\ell}$, can be related as:

$$\frac{s - s_i}{s_f - s_i} = \frac{\overline{m}N_{\ell\ell} - \overline{m}(N_{\ell\ell})_i}{\overline{m}(N_{\ell\ell})_f - \overline{m}(N_{\ell\ell})_i} ; \quad (50)$$

where \overline{m} is the mean mass of long-lived stars (including stellar remnants), $\overline{m} = M_s/N_{\ell\ell}$. Under the assumption of a universal stellar initial mass function, the fraction of long-lived stars belonging to a selected spectral class with respect to the total, maintains unchanged, $N_{\ell\ell}/N = \text{const}$, and Eq. (50) translates into (Pagel and Patchett 1975):

$$\frac{s - s_i}{s_f - s_i} = \frac{N - N_i}{N_f - N_i} ; \quad (51)$$

and the combination of Eqs. (31) and (32) yields:

$$(1 + \kappa)s = 1 - \mu ; \quad (52)$$

accordingly, Eq. (51) may be cast under the equivalent form:

$$\frac{N - N_i}{N_f - N_i} = \frac{1 - \mu/\mu_i}{1 - \mu_f/\mu_i} ; \quad (53)$$

where the ratio, μ/μ_i , is expressed by Eq. (28) with respect to the oxygen abundance, Z_O , and by Eqs. (44) and (46) with respect to the dimensionless cosmic time, \tilde{t} .

In terms of the normalized oxygen abundance, $\phi = Z_O/(Z_O)_\odot$, Eq. (28) translates into:

$$\phi - \phi_i = -\frac{\hat{p}''}{(Z_O)_\odot} \ln \frac{\mu}{\mu_i} ; \quad (54a)$$

$$\left| \hat{p}'' \ln \frac{\mu}{\mu_i} \right| < \left| \hat{p}'' \ln \frac{\mu_f}{\mu_i} \right| \ll 1 ; \quad (54b)$$

and the derivation of Eqs. (51) and (53) with respect to ϕ yields:

$$\frac{dN}{(N_f - N_i) d\phi} = \frac{ds}{(s_f - s_i) d\phi} = \frac{-d(\mu/\mu_i)}{(1 - \mu_f/\mu_i) d\phi} ; \quad (55)$$

which, using Eq. (54), takes the explicit form:

$$\frac{dN}{(N_f - N_i) d\phi} = \frac{\mu_i}{\mu_i - \mu_f} \frac{(Z_O)_\odot}{\hat{p}''} \exp \left[-\frac{(Z_O)_\odot}{\hat{p}''} (\phi - \phi_i) \right] ; \quad (56)$$

where the decimal logarithm of the left-hand side is defined as the TDOD (Pagel 1989; C00; C01):

$$\psi(\phi) = \log \frac{dN}{(N_f - N_i) d\phi} = a\phi + b ; \quad (57)$$

$$a = -\frac{1}{\ln 10} \frac{(Z_O)_\odot}{\hat{p}''} = -\frac{1}{\ln 10} \frac{(Z_O)_\odot}{\hat{p}} (1 + \kappa) ; \quad (58)$$

$$b = \log \left[\frac{\mu_i}{\mu_i - \mu_f} (-\ln 10) a \right] - a\phi_i ; \quad (59)$$

which is represented by a straight line on the $(O\phi\psi)$ plane.

The TDOD slope, a , defined by Eq. (58), depends on the flow regime discussed above. More specifically, $a < 0$ both in outflow regime and in moderate inflow regime; $a = 0$ in steady inflow regime; $a > 0$ in strong inflow regime. The TDOD intercept, b , defined by Eq. (59), must necessarily fulfill the condition, $\mu_f > 0$, which implies the inequality:

$$b > b(\mu_f = 0) = \log(-\ln 10 a) - a\phi_i ; \quad a < 0 ; \quad (60)$$

on the other hand, $\mu_f > 0$ directly follows from $a \geq 0$.

3.3 Fitting to empirical differential oxygen abundance distribution (EDOD)

Both the EDOD and the TDOD can be represented on the $(O\phi\psi)$ plane, but related normalizations are different. More specifically, the former is normalized to the sample population, N , according to Eq. (8), while the latter is normalized to the computed long-lived star population, $N_f - N_i$, according to Eq. (57). Then the EDOD and the TDOD differ by a normalization constant, $\log C_N$, which must be taken into consideration in performing the fitting procedure. In other words, the TDOD, ψ_T , has to be vertically shifted on the $(O\phi\psi)$ plane by a value, $\log C_N$, for matching to the EDOD, ψ_E . The TDOD intercept, defined by Eq. (59), translates into:

$$b = \log \left[\frac{C_N \mu_i}{\mu_i - \mu_f} (-\ln 10) a \right] - a\phi_i ; \quad (61)$$

where a and b can be determined as the EDOD regression line slope and intercept, respectively.

Using Eq. (58), the empirical counterpart of Eq. (27), which implies the validity of Eq. (54), reads:

$$\left| \frac{(Z_O)_\odot}{\ln 10} \frac{1}{a} \ln \frac{\mu}{\mu_i} \right| < \left| \frac{(Z_O)_\odot}{\ln 10} \frac{1}{a} \ln \frac{\mu_f}{\mu_i} \right| \ll 1 \quad ; \quad (62)$$

keeping in mind that the active gas mass fraction, μ , monotonically changes as a function of the normalized oxygen abundance, ϕ , for simple CBR models.

The particularization of Eq. (54) to the final configuration, by use of Eq. (58), reads:

$$\phi_f - \phi_i = \frac{1}{\ln 10} \frac{1}{a} \ln \frac{\mu_f}{\mu_i} \quad ; \quad (63)$$

and the combination of Eqs. (61) and (63) yields:

$$C_N = -\frac{1}{\ln 10} \frac{1}{a} \exp_{10}(a\phi_i + b) \{1 - \exp_{10}[a(\phi_f - \phi_i)]\} \quad ; \quad (64)$$

which may be determined from the knowledge of the EDOD and related regression line.

3.4 Different stages of evolution

The mere existence of a G-dwarf problem in different regions of the Galaxy (e.g., van den Bergh 1962; Schmidt 1963; H76; Prantzos 2003; Ferreras et al. 2003) and perhaps in all galaxies (Worthey et al. 1996; Henry and Worthey 1999) implies the EDOD cannot be fitted by a straight line, as predicted by simple CBR models, but by a continuous broken line at most. To this aim, simple CBR models shall be extended by allowing different flow regimes during different stages of evolution, and defined as simple multistage closed-(box+reservoir) (MCBR) models. Accordingly, the flow, κ , is different in different stages, while the equations of the model maintain their formal expression where variables and parameters are indexed by a letter, $U = \text{I, II, III, ...}$, which denotes the stage under consideration.

With regard to the U -th stage, the TDOD, defined by Eq. (57), reads:

$$\psi_U(\phi_U) = \log \frac{(C_U)_N ds_U}{[(s_U)_f - (s_U)_i] d\phi_U} \quad ; \quad (65)$$

where $(s_U)_i$ and $(s_U)_f$ are the fractional star mass at the beginning and at the end, respectively, of the U -th stage, and $\log(C_U)_N$ is the related normalization constant with respect to the EDOD, under the assumption of a

universal stellar initial mass function, according to Eq. (51). The combination of Eqs. (51), (56), and (65) yields:

$$\psi_U(\phi_U) = a_U \phi_U + b_U \quad ; \quad (66)$$

$$a_U = -\frac{1}{\ln 10} \frac{(Z_O)_\odot}{\hat{p}_U''} = -\frac{1}{\ln 10} \frac{(Z_O)_\odot}{\hat{p}_U} (1 + \kappa_U) \quad ; \quad (67)$$

$$b_U = \log \left[\frac{(C_U)_N (\mu_U)_i}{(\mu_U)_i - (\mu_U)_f} (-\ln 10) a_U \right] - a_U (\phi_U)_i \quad ; \quad (68)$$

which is valid provided the following inequality holds:

$$\left| \frac{(Z_O)_\odot}{\ln 10} \frac{1}{a_U} \ln \frac{\mu_U}{(\mu_U)_i} \right| < \left| \frac{(Z_O)_\odot}{\ln 10} \frac{1}{a_U} \ln \frac{(\mu_U)_f}{(\mu_U)_i} \right| \ll 1 \quad ; \quad (69)$$

in agreement with Eq. (62).

The particularization of Eq. (63) to the U-th stage reads:

$$(\phi_U)_f - (\phi_U)_i = \frac{1}{\ln 10} \frac{1}{a_U} \ln \frac{(\mu_U)_f}{(\mu_U)_i} \quad ; \quad (70)$$

and the combination of Eqs. (67), (68), and (70) yields:

$$(C_U)_N = -\frac{1}{\ln 10} \frac{1}{a_U} \exp_{10}[a_U (\phi_U)_i + b_U] \{1 - \exp_{10}\{a_U [(\phi_U)_f - (\phi_U)_i]\}\} \quad ; \quad (71)$$

which may be determined from the knowledge of the EDOD belonging to the U-th stage and related regression line. In general, different samples and/or different stages imply different values of the normalization constant.

3.5 Application to a special stellar system

For selected [O/H]-[Fe/H] relations, the EDOD related to the fs10 sample (taken as representative of the inner Galactic halo) can be divided into four or three regions where the trend is linear to a good extent, as shown in Figs. 4 and 5. In the light of the model, region A corresponds to the first stage of evolution, where the system is still assembling, characterized by strong inflow regime ($\kappa < -1$, $a > 0$); region F corresponds to the second stage of evolution, where the system is forming, characterized by outflow regime ($\kappa > 0$, $a < 0$); region C corresponds to the third stage of evolution, where the system is undergoing contraction, characterized by outflow regime; region E corresponds to the fourth step of evolution, where the system has attained dynamical equilibrium, characterized by outflow regime.

The gas and star mass fraction are left unchanged passing from a selected stage to the next one, which implies the validity of the following relations:

$$(X_U)_f = (X_V)_i ; \quad (X_A)_i = X_i ; \quad (X_E)_f = X_f ; \quad (72a)$$

$$X = \mu, s, D ; \quad U = A, F, C ; \quad V = F, C, E ; \quad (72b)$$

where X_i , X_f , are related to the whole evolution regardless of the stages. Accordingly, mass conservation during the U-th stage may be expressed as:

$$\mu_U + (1 + \kappa_U)s_U = \mu_U + s_U + D_U = (\mu_U)_i + (s_U)_i + (D_U)_i ; \quad (73)$$

where the initial values are known via Eq. (72).

The regression line in an assigned region of the EDOD is defined by the slope, a_U , and the intercept, b_U , and the intersections between regression lines related to adjacent regions mark initial and final values of normalized oxygen abundance, $(\phi_U)_i$ and $(\phi_U)_f$. The normalization constant, $(C_U)_N$, is determined via Eq. (71). The final value of the active gas mass fraction, $(\mu_U)_f$, follows from Eq. (70).

The yield, \hat{p} , and the lock, α , depend on the birth-rate stellar function. For a power-law stellar initial mass function, the EDOD in different Galactic environments is reproduced to a good extent from simple CBR models with the following output parameters (CM09):

$$\frac{\hat{p}}{(Z_O)_\odot} = 1.0340 ; \quad (74a)$$

$$\alpha_{2.9} = 0.66604 ; \quad \alpha_{2.35} = 0.85360 ; \quad (74b)$$

$$(\widetilde{m}_{mf})_{2.9} = 0.44449 ; \quad (\widetilde{m}_{mf})_{2.35} = 0.015436 ; \quad (74c)$$

for an assumed solar oxygen abundance, $(Z_O)_\odot = 0.0056$, where the indices relate to power-law exponents equal to 2.9 and 2.35, respectively. For further details refer to earlier attempts (C01; C07).

The flow, κ_U , is deduced from Eq. (67). The final star mass fraction, $(s_U)_f$, and outflowed or inflowed gas mass fraction, $(D_U)_f$, are determined from Eq. (73) particularized to the end of the U-th stage.

In the light of the model, the initial star mass fraction, s_i , results from the fractional mass in stars (including stellar remnants) with normalized oxygen abundance, $\phi < \phi_i$. The above value, though still uncertain at present, may be underestimated to a good extent as $s_i = 0$. In addition, $D_i = 0$ without loss of generality, which implies $\mu_i = 1$.

The fractional mass of the box (with respect to the initial value) attains the maximum value at the end of A stage, where gas inflows into the box from the reservoir. The related value is $(\mu_A)_f + (s_A)_f$. The fractional mass

in stars at the end of evolution, which coincides with the end of E stage, is $(s_E)_f$. Accordingly, the mass ratio of the box at the end of evolution to the outflowed gas reads:

$$\frac{M_{\text{box}}}{M_{\text{off}}} = \frac{(\mu_E)_f + (s_E)_f}{(\mu_A)_f + (s_A)_f - (\mu_E)_f - (s_E)_f} ; \quad (75)$$

provided the earlier stage A is in inflow regime and the subsequent stages F, C, (or FC), E, are in outflow regime, as it is the case for the EDOD and related TDOD under consideration.

With the above values of input parameters, the flow, the active gas mass fraction, the star mass fraction, and the outflowed or inflowed gas mass fraction, at the end of each stage of evolution, can be computed. The results are listed in Table 7 for the EDOD related to the fs10 sample for [O/H]-[Fe/H] empirical relations deduced from the RB09 sample (top panel) and Fal09 sample, case SH1 (middle and bottom panel), see Fig. 4. With regard to the bottom panel, stages F and C are merged into a single one, FC.

In the former case (top panel), where the empirical [O/H]-[Fe/H] relation has been determined using the LTE approximation (RB09), the mass of the box is increased by a factor of about 10 at the end of A stage, and is reduced to about the initial value at the end of E stage. The mass ratio, $M_{\text{box}}/M_{\text{off}}$, is about one tenth via Eq. (75).

In the latter case (middle and bottom panel), where the empirical [O/H]-[Fe/H] relation has been determined relaxing the LTE approximation (Fal09), the mass of the box is increased by a factor of about 3-4 at the end of A stage, and is reduced to about one half the initial value at the end of E stage. The mass ratio, $M_{\text{box}}/M_{\text{off}}$, is about one sixth via Eq. (75).

In any case, the initial mass of the box at the beginning of A stage (proto-inner halo) is comparable to the mass of the box at the end of E stage (present inner halo).

3.6 Discussion

Though TDODs calculated using simple MCBR models of chemical evolution fit to EDODs with different linear trends in different regions, as shown in Fig. 5, still the application to the inner Galactic halo remains speculative in absence of further improvement. The main reasons are outlined below.

First, the EDOD has been derived from a fictitious sample, fs10, which, in turn, has been deduced from two incomplete samples, RN91 and H V, both biased (to a different extent) towards low metallicities and affected by disk contamination. A homogeneous and unbiased sample would be needed to

Table 7: Input parameters (deduced from the regression lines), $(\phi_U)_i$, a_U , b_U , and output parameters, κ_U , $(\mu_U)_f$, $(s_U)_f$, $(D_U)_f$, for simple MCBR models fitting to the EDOD related to the fs10 sample, for [O/H]-[Fe/H] empirical relations deduced from the RB09 sample (top panel) and Fal09 sample, case SH1 (middle and bottom panel). Four (A, F, C, E; top and middle panels) or three (A, FC, E; bottom panel) stages of evolution are considered, according to the linear trends exhibited by the EDOD (Fig. 4). Stages O before A and after E are not considered as no sample object lies within the corresponding metallicity range. Other input parameters are $(Z_O)_\odot = 0.0056$; $\hat{p}/(Z_O)_\odot = 1.0340$; $\mu_i = (\mu_O)_f = 1$; $s_i = (s_O)_f = 0$; $D_i = (D_O)_f = 0$; where the index, O, denotes oxygen with regard to the solar abundance and stage O of evolution otherwise. For further details refer to the text.

U	$(\phi_U)_i$	a_U	b_U	κ_U	$(\mu_U)_f$	$(s_U)_f$	$(D_U)_f$
A	9.4624E-4	+1.1382E+2	-1.0567E-1	-2.7201E+2	9.9175E-0	3.2905E-2	-8.9
F	9.7001E-3	-2.0950E+0	+1.0188E-0	+3.9881E+0	7.7178E-0	4.7391E-1	-7.1
C	6.1687E-2	-7.3565E+0	+1.3433E-0	+1.6515E+1	4.5710E-1	8.8844E-1	-3.4
E	2.2854E-1	-2.2569E+0	+1.7784E-1	+4.3735E+0	3.5961E-2	9.6681E-1	-2.7
O	7.1779E-1						
A	3.1623E-4	+7.9432E+1	+2.7571E-1	-1.9012E+2	3.6714E-0	1.4125E-2	-2.6
F	7.4271E-3	-3.8855E+0	+8.9453E-1	+8.2913E+0	1.2551E-0	2.7531E-1	-5.3
C	1.2740E-1	-2.6460E+0	+7.3661E-1	+5.3000E+0	5.4973E-2	4.6581E-1	+4.7
E	6.4083E-1	-5.3661E-1	-6.1514E-1	+2.7764E-1	2.4384E-3	5.0693E-1	+4.9
O	3.1623E-0						
A	3.1623E-4	+7.9432E+1	+2.5751E-1	-1.9012E+2	3.2209E-0	1.1743E-2	-2.2
FC	6.7114E-3	-2.8643E+0	+8.2804E-1	+5.8196E+0	5.6405E-2	4.7577E-1	+4.6
E	6.2002E-1	-5.3661E-1	-6.1514E-1	+4.7764E-1	2.4384E-3	5.1801E-1	+4.7
O	3.1623E-0						

this respect. The EDOD high-metallicity tail could be largely due to disk contamination as stage E begins at $[\text{Fe}/\text{H}] \approx -1$, which is close to both the transition from halo to bulge/disk globular cluster (e.g., Mackey and van den Bergh 2005) and the peak of bulge EDOD (Sadler et al. 1996). Different linear trends in different regions are also shown by globular clusters (C07), bulge (C07), and disk (Caimmi 2008) EDOD.

A linear trend exhibited by the EDOD related to different Galactic environments or galactic environments provided the G-dwarf problem is universal (Worthey et al. 1996; Henry and Worthey 1999), implies outflowing or inflowing gas with same composition as the preexisting gas. If the above mentioned effect is real, the chemical evolution within the building blocks of galactic subsystems, in particular the inner Galactic halo, occurred to a similar extent.

Second, using different methods yields different $[\text{O}/\text{H}]-[\text{Fe}/\text{H}]$ empirical relations, as shown in Fig. 3, even in dealing with coinciding sample objects, as listed in Table 1. With regard to the inner Galactic halo, the initial mass deduced using two selected $[\text{O}/\text{H}]-[\text{Fe}/\text{H}]$ empirical relations, has been found to change by a factor of about two. Future improvement would imply direct oxygen abundance determinations (Ramirez et al. 2007) where different methods yield consistent results or, at least, a $[\text{O}/\text{H}]-[\text{Fe}/\text{H}]$ empirical relation which attains general consensus.

Third, though the assumption of null star mass fraction holds to a good extent for the starting configuration, still the presence of stars with lower metallicity with respect to sample objects, $[\text{Fe}/\text{H}] < -4.2$, has to be considered. This extremely low metallicity has currently been detected in about a dozen of stars down to $[\text{Fe}/\text{H}] \approx -5.4$ (e.g., Beers and Christlieb 2005). Basing on theoretical arguments, a lower limit oxygen abundance in Pop II stars has been determined as $[\text{O}/\text{H}] = -3.05 \pm 0.20$ (Bromm and Loeb 2003), where earlier nucleosynthesis comes from more massive Pop III stars.

If the transition from the latter to the former population was not instantaneous, and coeval Pop III and Pop II stars were generated (Smith et al. 2009), then the stellar initial mass function can no longer be considered as universal in time for Pop II stars. Accordingly, model evolution must be started after the last Pop III star has undergone supernova explosion, which has been assumed to take place when the metal abundance is $[\text{Fe}/\text{H}] = -4.2$. In absence (to the knowledge of the author) of a reliable estimate of the mass fraction in stars and stellar remnants with initial metal abundance, $[\text{Fe}/\text{H}] < -4.2$, a null value has been assigned.

For a stellar system resembling the inner Galactic halo, a nontrivial question is concerned with the nature of the reservoir where gas outflows after the assembling (A) stage. A natural candidate is the bulge, as suggested by

comparison between specific angular momentum distributions related to halo and bulge stars (Wyse and Gilmore 1992). According to recent attempts, (1) the Galactic halo is made of an inner component which exhibits a modest prograde rotation and a metallicity peak at $[\text{Fe}/\text{H}] \approx -1.6$, and an outer component which exhibits a clear retrograde net rotation and a metallicity peak at $[\text{Fe}/\text{H}] \approx -2.2$ (Carollo et al. 2007, 2010); and (2) the Galactic bulge is made of an inner component which exhibits bar-like kinematics and metal-rich population, and an outer component which exhibits spheroid kinematics and metal-poor population (Babusiaux et al. 2010). Then a similar specific angular momentum distribution related to inner halo and outer bulge is expected.

In this view, the mass ratio of the box at the end of evolution to the gas outflowed from the box into the reservoir during the evolution, $M_{\text{box}}/M_{\text{off}}$, expressed by Eq. (75), should reproduce the mass ratio of (inner) halo to (outer) bulge, as:

$$\frac{(M_{\text{H}})_{\text{inn}}}{(M_{\text{B}})_{\text{out}}} = \frac{(M_{\text{H}})_{\text{inn}}/M_{\text{H}}}{(M_{\text{B}})_{\text{out}}/M_{\text{B}}} \frac{M_{\text{H}}}{M_{\text{B}}} ; \quad (76)$$

which is equivalent to:

$$\frac{(M_{\text{H}})_{\text{inn}}}{M_{\text{H}}} = \frac{(M_{\text{H}})_{\text{inn}}/(M_{\text{B}})_{\text{out}}}{M_{\text{H}}/M_{\text{B}}} \frac{(M_{\text{B}})_{\text{out}}}{M_{\text{B}}} ; \quad (77)$$

where the indices, inn and out, denote the inner and the outer component, respectively, H the halo, and B the bulge. The inner halo to the outer bulge mass ratio, deduced from the results listed in Table 7, is $(M_{\text{H}})_{\text{inn}}/(M_{\text{B}})_{\text{out}} \approx 0.10\text{-}0.20$. The halo to bulge mass ratio is currently estimated as $M_{\text{H}}/M_{\text{B}} \approx 0.05\text{-}0.10$. Then simple MCBR models considered here yield an inner halo fractional mass (normalized to the halo) which is comparable with, or exceeding by a factor up to 4, the outer bulge fractional mass (normalized to the bulge). On the other hand, quantitative results cannot be expected for the above mentioned reasons. In conclusion, the (inner) halo to (outer) bulge mass ratio appears to be an additional output parameter provided by simple MCBR models of chemical evolution, with regard to the inner Galactic halo.

In the light of the model, the inner Galactic halo can be considered independently of the outer halo and the bulge for the following reasons. The outer halo is both dynamically and chemically decoupled from the inner halo (Carollo et al. 2010), which implies accretion by smaller subunits (mainly dwarf spheroidal galaxies) after the formation of the inner halo. In fact, globular clusters belonging to the inner and outer halo are usually classified as “old halo” and “young halo”, respectively (e.g., Mackey and van den

Bergh 2005). Similarly, a (inner) halo - (metal-poor) bulge collapse can be inferred by comparison of related specific angular momentum distributions (Wise and Gilmore 1992), which implies bulge formation is subsequent to inner halo formation, and then the (metal-poor) bulge may be considered as a reservoir for the outflowing gas, in the sense specified by the model.

4 Conclusion

Under the assumption that two samples of halo stars, RN91 and H V, are equally representative of the inner Galactic halo within the metallicity range, $-3.0 \leq [\text{Fe}/\text{H}] \leq -2.8$, a fictitious sample, fs10, has been built up and taken as representative of the inner Galactic halo within the metallicity range, $-4.2 \leq [\text{Fe}/\text{H}] \leq +0.2$. The related differential empirical oxygen abundance distribution (EDOD) has been established using different $[\text{O}/\text{H}]-[\text{Fe}/\text{H}]$ empirical relations, deduced from different samples (RB09, Fal09, Sal09) where different methods have been exploited for determining the oxygen abundance.

More precisely, the EDOD has been deduced from the fs10 sample by use of two alternative $[\text{O}/\text{H}]-[\text{Fe}/\text{H}]$ empirical relations: one, determined from the RB09 sample in presence of local thermodynamical equilibrium (LTE) approximation (RB09), and one other, determined from the Fal09 sample in absence of LTE approximation with due account taken of the inelastic collisions via neutral H atoms, SH1 (Fal09, $S_{\text{H}} = 1$), as shown in Fig. 3.

A linear trend has been exhibited by related EDODs within three or four regions, as shown in Fig. 4, and the slope and intercept estimators of corresponding regression lines have been determined together with their dispersions, as listed in Table 2 using different interpolation methods. It has been pointed out that the earlier trend, characterized by positive slope, is a signature of a G-dwarf problem.

The main uncertainties on the EDOD have been recognized as related to (1) biases on the RN91 and H V samples due to selection effects towards sufficiently low ($[\text{Fe}/\text{H}] < -4.2$) and sufficiently high ($[\text{Fe}/\text{H}] > -2.8$) metal abundance (H V) and disk contamination for $[\text{Fe}/\text{H}] > -2.0$ (RN91; H V), and (2) lack of clear indications on a recommended method for determining oxygen abundance, as shown in Table 1 and in Fig. 1 for 11 stars in common among the RB09 and the Fal09 sample.

Fitting a theoretical differential oxygen abundance distribution (TDOD) to the above discussed EDOD has needed an extension of simple closed-box (CB) models of chemical evolution on two respects. First, the system has been conceived as made of a box and a reservoir, where the following processes have been allowed: gas outflow from the box into the reservoir (H76),

moderate gas inflow (C07), steady and strong gas inflow (current paper) into the box from the reservoir. Simple closed-(box+reservoir) (CBR) models have exhibited mass conservation within the system (box+reservoir), while it has been violated within a single subsystem (box or reservoir). Second, the history of the system has been conceived as a succession of different stages characterized by different outflow or inflow rate. Simple multistage closed-(box+reservoir) (MCBR) models have been found to yield TDODs in the form of continuous broken lines, which can fit to related EDODs.

An application of MCBR models to a special stellar system resembling the inner Galactic halo has been made with fiducial values of input parameters which cannot be deduced from the EDOD. The metal abundance at the beginning and at the end of each stage, have been inferred from the intersection of regression lines fitting to adjacent regions of the EDOD, as shown in Fig. 5. The mass ratio of the box at the end of evolution to the gas outflowed from the box into the reservoir through the evolution, has been determined as $M_{\text{box}}/M_{\text{off}} \approx 0.11$ for a [O/H]-[Fe/H] empirical relation deduced from the RB09 sample in presence of LTE approximation (RB09), and $M_{\text{box}}/M_{\text{off}} \approx 0.16\text{-}0.19$ for a [O/H]-[Fe/H] empirical relation deduced from the Fal09 sample in absence of LTE approximation with due account taken of the inelastic collisions via neutral H atoms, SH1 (Fal09, $S_{\text{H}} = 1$), with regard to four and three stages of evolution, respectively.

For current estimates of the halo-to-bulge mass ratio, $M_{\text{halo}}/M_{\text{bulge}} \approx 0.05\text{-}0.10$, the inner halo fractional mass (normalized to the halo) has been found to be comparable with, or exceeding by a factor up to 4, the metal-poor bulge fractional mass (normalized to the bulge). On the other hand, it has been considered that quantitative predictions cannot be made for the Galaxy unless complete and unbiased samples of the inner Galactic halo are available, and discrepancies among [O/H]-[Fe/H] empirical relations related to different samples and different methods are removed.

References

- [1] Babusiaux, C., Gomez, A, Hill, V., et al.: 2007, *Astron. Astrophys.*, 519, A77.
- [2] Barbuy, B., Nissen, P.E., Peterson, R., Spite, F. (eds.): 2001, *Proceedings of Oxygen abundances in Old Stars and Implications for Nucleosynthesis and Cosmology* (IAU Joint Discussion 8), *New Astron. Rev.*, 45, 509.
- [3] Beers, T.C., Christlieb, D.: 2005, *Ann. Rev. Astron. Astrophys.*, 43, 531.

- [4] Bromm, V., Loeb, A.: 2003, *Nature*, 425, 812.
- [5] Caimmi, R.: 2000, *Astron. Nachr.*, 321, 323. (C00).
- [6] Caimmi, R.: 2001a, *Astron. Nachr.*, 322, 65. (C00, erratum).
- [7] Caimmi, R.: 2001b, *Astron. Nachr.*, 322, 241. (C01).
- [8] Caimmi, R.: 2007, *New Astron.*, 12, 289. (C07).
- [9] Caimmi, R.: 2008, *New Astron.*, 13, 314.
- [10] Caimmi, R., Milanese, E.: 2009, *Astrophys. Space Sci.*, 323, 147. (CM09).
- [11] Carollo, D., Beers, T.C., Lee, Y.S., et al.: 2007, *Nature*, 318, 1020.
- [12] Carollo, D., Beers, T.C., Chiba, M., et al.: 2010, *Astrophys. J.*, 712, 692.
- [13] Fabbian, D., Nissen, P.E., Asplund, M., et al.: 2009, *Astron. Astrophys.*, 500, 1143. (Fal09).
- [14] Feigelson, E.D., Babu, G.J.: 1992, *Astrophys. J.*, 397, 55.
- [15] Ferreras, I., Wyse, R.F.G., Silk, J.: 1999, *Mon. Not. R. Astron. Soc.*, 345, 1381.
- [16] Hartwick, F.D.A.: 1976, *Astrophys. J.*, 209, 418. (H76).
- [17] Haywood, M.: 2001, *Mon. Not. R. Astron. Soc.*, 325, 1365.
- [18] Henry, R.B.C., Worthey, G.: 1999, *Publ. Astron. Soc. Pac.*, 111, 919.
- [19] Isobe, T., Feigelson, E.D., Akritas, M.G., Babu, G.J.: 1990, *Astrophys. J.*, 364, 104.
- [20] Li, H.N., Christlieb, N., Schörck, T., et al.: 2010, *Astron. Astrophys.*, 521, A10.
- [21] Mackey, A.D., van den Bergh, S.: 2005, *Mon. Not. R. Astron. Soc.*, 360, 631.
- [22] Malinie, G., Hartmann, D.H., Clayton, D.D., Mathews, G.J.: 1993, *Astrophys. J.*, 413, 633.

- [23] Melendez, J., Asplund, M., Alves-Brito, A., et al.: 2008, *Astron. Astrophys.*, 484, L21.
- [24] Pagel, B.E.J.: 1989, The G-dwarf Problem and Radio-active Cosmochronology. In: Beckman J.E., Pagel B.E.J. (eds.) *Evolutionary Phenomena in Galaxies*, p.201. Cambridge University Press, Cambridge.
- [25] Pagel, B.E.J., Patchett, B.E.: 1975, *Mon. Not. R. Astron. Soc.*, 172, 13.
- [26] Prantzos, N.: 2003, *Astron. Astrophys.*, 404, 211.
- [27] Prantzos, N.: 2007, The Chemical Evolution of the Milky Way in a cosmological context, *EAS Publications Series*, 24, 3.
- [28] Ramirez, I., Allende Prieto, C., Lambert, D.L.: 2007, *Astron. Astrophys.*, 465, 271.
- [29] Rich, J.A., Boesgaard, A.M.: 2009, *Astrophys. J.*, 701, 519. (RB09).
- [30] Rocha-Pinto, H.J., Maciel, W.J.: 1996, *Mon. Not. R. Astron. Soc.*, 279, 447.
- [31] Ryan, S.G., Norris, J.E.: 1991, *Astron. J.*, 101, 1865. (RN91).
- [32] Sadler, E.M., Rich, R.M., Terndrup, D.M.: 1996, *Astron. J.*, 112, 171.
- [33] Schmidt, M.: 1959, *Astrophys. J.*, 129, 243.
- [34] Schmidt, M.: 1963, *Astrophys. J.*, 137, 758.
- [35] Schmidt, S.J., Wallerstein, G., Woolf, V.M., Bean, J.L.: 2009, *Pub. Astron. Soc. Pac.*, 121, 1083. (Sal09).
- [36] Schörck, T., Christlieb, N., Cohen, J.G., et al.: 2009, *Astron. Astrophys.*, 507, 817. (H V).
- [37] Searle, L., Sargent, W.L.W.: 1972, *Astrophys. J.*, 173, 25.
- [38] Smith, B.D., Tuck, M.J., Sigurdsson, S., et al.: 2009, *Astrophys. J.*, 691, 441.
- [39] Truran, J.W., Cameron, A.G.W.: 1971, *Astrophys. Space Sci.*, 14, 179.
- [40] van den Bergh, S.: 1962, *Astrophys. J.*, 67, 486.
- [41] Wang, B., Silk, J.: 1993, *Astrophys. J.*, 406, 580.

- [42] Worthey, G., Dorman, B., Jones, L.A.: 1996, *Astron. J.*, 112, 948.
- [43] Wyse, R.F.G., Gilmore, G.: 1992, *Astron. J.*, 104, 144.
- [44] York, D.: 1966, *Canadian J. Phys.*, 44, 1079.

Appendix

A Tables

Tables 3, 4, and 7 may be exceedingly large in the text, and for this reason they are broken to be completely accessible.

Table 8: Table 3, left.

		[O/H] = 0.72 [Fe/H] (RB09)			
B_F^-	B_F^+	B_O^-	B_O^+	ϕ	$\Delta^\mp \phi$
-4.2	-4.0	-3.024	-2.880	1.1322D-3	1.8601D-4
-4.0	-3.8	-2.880	-2.736	1.5774D-3	2.5914D-4
-3.8	-3.6	-2.736	-2.592	2.1976D-3	3.6102D-4
-3.6	-3.4	-2.592	-2.448	3.0615D-3	5.0296D-4
-3.4	-3.2	-2.448	-2.304	4.2652D-3	7.0071D-4
-3.2	-3.0	-2.304	-2.160	5.9421D-3	9.7619D-4
-3.0	-2.8	-2.160	-2.016	8.2783D-3	1.3600D-3
-2.8	-2.6	-2.016	-1.872	1.1533D-2	1.8947D-3
-2.6	-2.4	-1.872	-1.728	1.6067D-2	2.6396D-3
-2.4	-2.2	-1.728	-1.584	2.2384D-2	3.6774D-3
-2.2	-2.0	-1.584	-1.440	3.1185D-2	5.1231D-3
-2.0	-1.8	-1.440	-1.296	4.3445D-2	7.1373D-3
-1.8	-1.6	-1.296	-1.152	6.0526D-2	9.9434D-3
-1.6	-1.4	-1.152	-1.008	8.4322D-2	1.3853D-2
-1.4	-1.2	-1.008	-0.864	1.1747D-1	1.9299D-2
-1.2	-1.0	-0.864	-0.720	1.6366D-1	2.6887D-2
-1.0	-0.8	-0.720	-0.576	2.2800D-1	3.7457D-2
-0.8	-0.6	-0.576	-0.432	3.1764D-1	5.2184D-2
-0.6	-0.4	-0.432	-0.288	4.4253D-1	7.2700D-2
-0.4	-0.2	-0.288	-0.144	6.1651D-1	1.0128D-1
-0.2	+0.0	-0.144	+0.000	8.5890D-1	1.4110D-1
+0.0	+0.2	+0.000	+0.144	1.1966D-0	1.9658D-1
+0.2	+0.4	+0.144	+0.288	1.6670D-0	2.7386D-1

Table 9: Table 3, right.

		[O/H] = [Fe/H] + 0.70		(Fal09)	
B_F^-	B_F^+	B_O^-	B_O^+	ϕ	$\Delta^\mp \phi$
-4.2	-4.0	-3.5	-3.3	4.0871D-4	9.2480D-5
-4.0	-3.8	-3.3	-3.1	6.4776D-4	1.4657D-4
-3.8	-3.6	-3.1	-2.9	1.0266D-3	2.3230D-4
-3.6	-3.4	-2.9	-2.7	1.6271D-3	3.6817D-4
-3.4	-3.2	-2.7	-2.5	2.5788D-3	5.8351D-4
-3.2	-3.0	-2.5	-2.3	4.0871D-3	9.2480D-4
-3.0	-2.8	-2.3	-2.1	6.4776D-3	1.4657D-3
-2.8	-2.6	-2.1	-1.9	1.0266D-2	2.3230D-3
-2.6	-2.4	-1.9	-1.7	1.6271D-2	3.6817D-3
-2.4	-2.2	-1.7	-1.5	2.5788D-2	5.8351D-3
-2.2	-2.0	-1.5	-1.3	4.0871D-2	9.2480D-3
-2.0	-1.8	-1.3	-1.1	6.4776D-2	1.4657D-2
-1.8	-1.6	-1.1	-0.9	1.0266D-1	2.3230D-2
-1.6	-1.4	-0.9	-0.7	1.6271D-1	3.6817D-2
-1.4	-1.2	-0.7	-0.5	2.5788D-1	5.8351D-2
-1.2	-1.0	-0.5	-0.3	4.0871D-1	9.2480D-2
-1.0	-0.8	-0.3	-0.1	6.4776D-1	1.4657D-1
-0.8	-0.6	-0.1	+0.1	1.0266D+0	2.3230D-1
-0.6	-0.4	+0.1	+0.3	1.6271D+0	3.6817D-1
-0.4	-0.2	+0.3	+0.5	2.5788D+0	5.8351D-1
-0.2	+0.0	+0.5	+0.7	4.0871D+0	9.2480D-1
+0.0	+0.2	+0.7	+0.9	6.4776D+0	1.4657D-0
+0.2	+0.4	+0.9	+1.1	1.0266D+1	2.3230D-0

Table 10: Table 4, left.

[O/H] = 0.72 [Fe/H] (RB09)				ΔN		
ϕ	ψ	$\Delta^- \psi$	$\Delta^+ \psi$	fs10	H V	RN91
1.1322D-3	-1.4181D-1	5.3329D-1	2.3226D-1	2	2	0
1.5774D-3				0	0	0
2.1976D-3				0	0	1
3.0615D-3	+2.0434D-1	1.4793D-1	1.1014D-1	12	12	1
4.2652D-3	+6.3437D-1	4.7712D-1	2.2185D-1	45	45	2
5.9421D-3	+7.0048D-1	3.2187D-1	1.8282D-1	73	73	2
8.2783D-3	+8.9728D-1	1.8947D-1	1.3148D-1	160	160	8
1.1533D-2	+9.6413D-1	1.4107D-1	1.0631D-1	260	198	13
1.6067D-2	+1.0284D-0	1.0691D-1	8.5725D-2	420	281	21
2.2384D-2	+9.4240D-1	9.9155D-2	8.0671D-2	480	337	24
3.1185D-2	+9.4967D-1	8.1707D-2	6.8742D-2	680	399	34
4.3445D-2	+9.1764D-1	7.0967D-2	6.0983D-2	880	313	44
6.0526D-2	+9.2258D-1	5.8986D-2	5.1924D-2	1240	231	62
8.4322D-2	+6.9376D-1	6.5516D-2	5.6916D-2	1020	229	51
1.1747D-1	+4.7566D-1	7.1860D-2	6.1640D-2	860	209	43
1.6366D-1	+1.4535D-1	9.0970D-2	7.5175D-2	560	308	28
2.2800D-1	-3.3187D-1	1.4107D-1	1.0631D-1	260	268	13
3.1764D-1	-5.1063D-1	1.4793D-1	1.1014D-1	240	178	12
4.4253D-1	-8.8871D-1	2.0618D-1	1.3924D-1	140	109	7
6.1651D-1	-1.1788D-0	2.5744D-1	1.6053D-1	100	45	5
8.5890D-1				0	33	0
1.1966D-0	-2.1658D-0	$+\infty$	3.0103D-1	20	3	1
1.6670D-0				0	6	0

Table 11: Table 4, right.

[O/H] = [Fe/H] + 0.70 (Fal09)				ΔN		
ϕ	ψ	$\Delta^- \psi$	$\Delta^+ \psi$	fs10	H V	RN91
4.0871D-4	+1.6168D-1	5.3329D-1	2.3226D-1	2	2	0
6.4776D-4				0	0	0
1.0266D-3				0	0	1
1.6271D-3	+3.3983D-1	1.4793D-1	1.1014D-1	12	12	1
2.5788D-3	+7.1386D-1	4.7712D-1	2.2185D-1	45	45	2
4.0871D-3	+7.2397D-1	3.2187D-1	1.8282D-1	73	73	2
6.4776D-3	+8.6477D-1	1.8947D-1	1.3148D-1	160	160	8
1.0266D-2	+8.7562D-1	1.4107D-1	1.0631D-1	260	198	13
1.6271D-2	+8.8390D-1	1.0691D-1	8.5725D-2	420	281	21
2.5788D-2	+7.4189D-1	9.9155D-2	8.0671D-2	480	337	24
4.0871D-2	+6.9316D-1	8.1707D-2	6.8742D-2	680	399	34
6.4776D-2	+6.0513D-1	7.0967D-2	6.0983D-2	880	313	44
1.0266D-1	+5.5407D-1	5.8986D-2	5.1924D-2	1240	231	62
1.6271D-1	+2.6925D-1	6.5516D-2	5.6916D-2	1020	229	51
2.5788D-1	-4.8510D-3	7.1860D-2	6.1640D-2	860	209	43
4.0871D-1	-3.9116D-1	9.0970D-2	7.5175D-2	560	308	28
6.4776D-1	-9.2438D-1	1.4107D-1	1.0631D-1	260	268	13
1.0266D+0	-1.1591D-0	1.4793D-1	1.1014D-1	240	178	12
1.6271D+0	-1.5932D-0	2.0618D-1	1.3924D-1	140	109	7
2.5788D+0	-1.9393D-0	2.5744D-1	1.6053D-1	100	45	5
4.0871D+0				0	33	0
6.4776D+0	-3.0383D-0	$+\infty$	3.0103D-1	20	3	1
1.0266D+1				0	6	0

Table 12: Table 7, left.

U	$(\phi_U)_i$	a_U	b_U
A	9.4624E-4	+1.1382E+2	-1.0567E-1
F	9.7001E-3	-2.0950E+0	+1.0188E-0
C	6.1687E-2	-7.3565E+0	+1.3433E-0
E	2.2854E-1	-2.2569E+0	+1.7784E-1
O	7.1779E-1		
A	3.1623E-4	+7.9432E+1	+2.7571E-1
F	7.4271E-3	-3.8855E+0	+8.9453E-1
C	1.2740E-1	-2.6460E+0	+7.3661E-1
E	6.4083E-1	-5.3661E-1	-6.1514E-1
O	3.1623E-0		
A	3.1623E-4	+7.9432E+1	+2.5751E-1
FC	6.7114E-3	-2.8643E+0	+8.2804E-1
E	6.2002E-1	-5.3661E-1	-6.1514E-1
O	3.1623E-0		

Table 13: Table 7, right.

U	κ_U	$(\mu_U)_f$	$(s_U)_f$	$(D_U)_f$
A	-2.7201E+2	9.9175E-0	3.2905E-2	-8.9504E-0
F	+3.9881E+0	7.7178E-0	4.7391E-1	-7.1917E-0
C	+1.6515E+1	4.5710E-1	8.8844E-1	-3.4554E-1
E	+4.3735E+0	3.5961E-2	9.6681E-1	-2.7737E-3
O				
A	-1.9012E+2	3.6714E-0	1.4125E-2	-2.6855E-0
F	+8.2913E+0	1.2551E-0	2.7531E-1	-5.3043E-1
C	+5.3000E+0	5.4973E-2	4.6581E-1	+4.7922E-1
E	+2.7764E-1	2.4384E-3	5.0693E-1	+4.9063E-1
O				
A	-1.9012E+2	3.2209E-0	1.1743E-2	-2.2327E-0
FC	+5.8196E+0	5.6405E-2	4.7577E-1	+4.6782E-1
E	+4.7764E-1	2.4384E-3	5.1801E-1	+4.7955E-1
O				

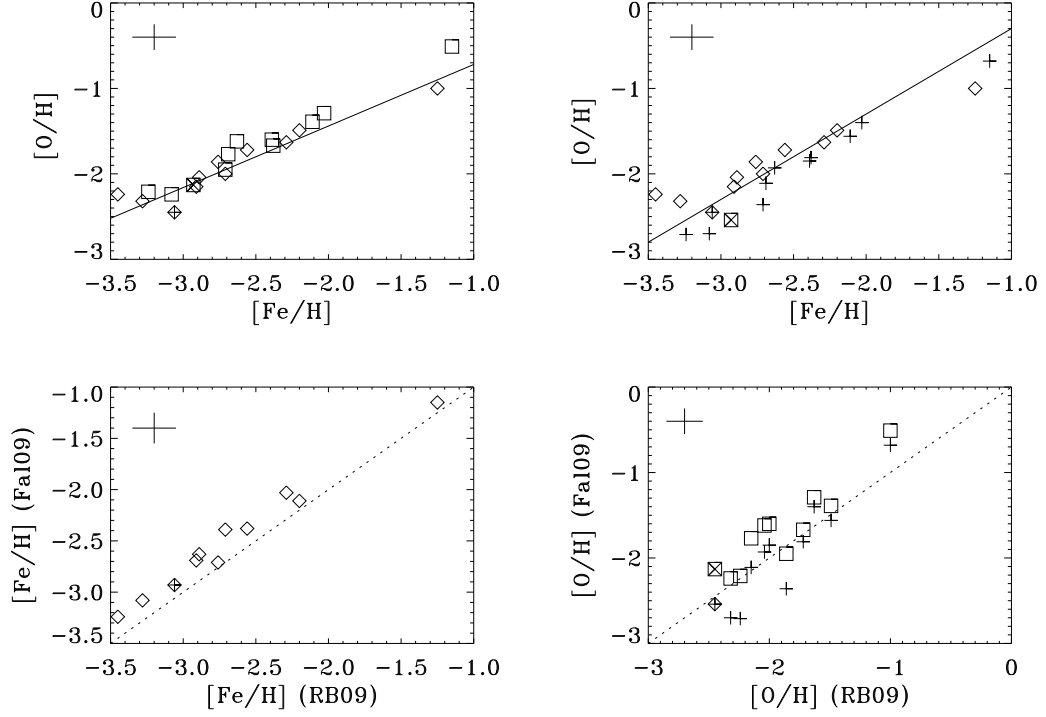


Figure 1: Comparison between (i) $[O/H]$ - $[Fe/H]$ empirical relations deduced from 11 halo stars in common among RB09 (upper panels, diamonds) and Fal09, case LTE (top left, squares), case SH1 (top right, crosses), and (ii) $[Fe/H]$ (bottom left) and $[O/H]$ (bottom right), case LTE (squares), case SH1 (crosses), deduced from the above mentioned stars. The composite symbols mark LP831-070, where only an upper limit to oxygen abundance is available in the Fal09 sample. The straight lines in upper panels are $[O/H] = 0.72[Fe/H]$ (left) and $[O/H] = [Fe/H] + 0.70$ (right). The 1:1 correspondence in lower panels is represented by a dashed line. Typical uncertainties are visualized as crosses on the top left corner of each panel.

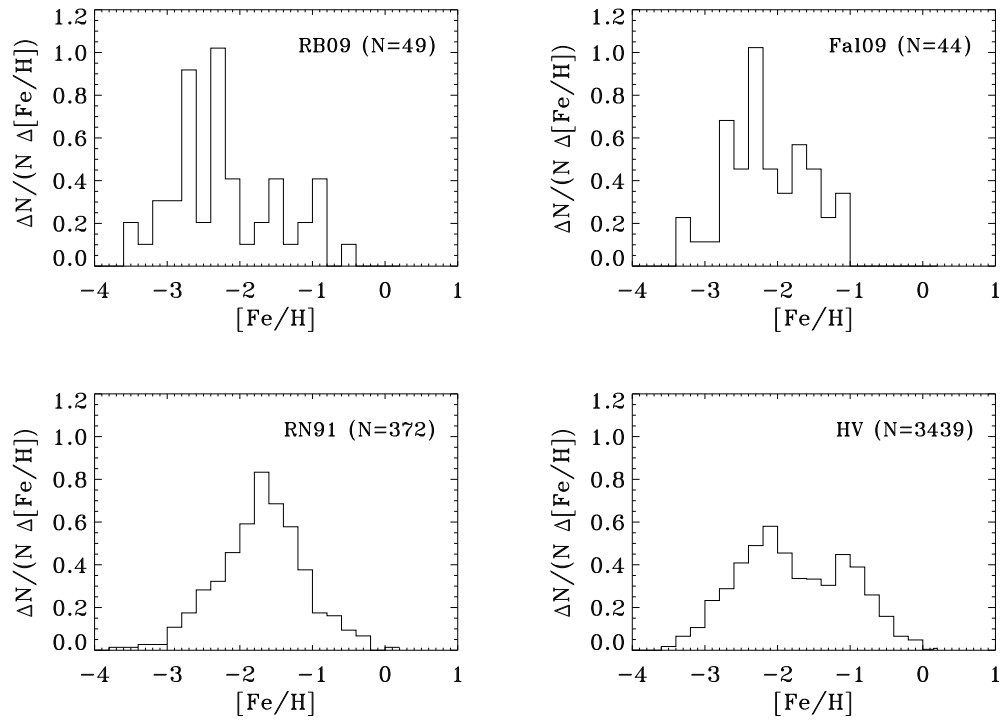


Figure 2: $[\text{Fe}/\text{H}]$ distributions (normalized to the unit area) related to four different samples discussed in the text. Sample denomination and population are indicated on each panel. In all cases, the bin width is $\Delta[\text{Fe}/\text{H}] = 0.2$.

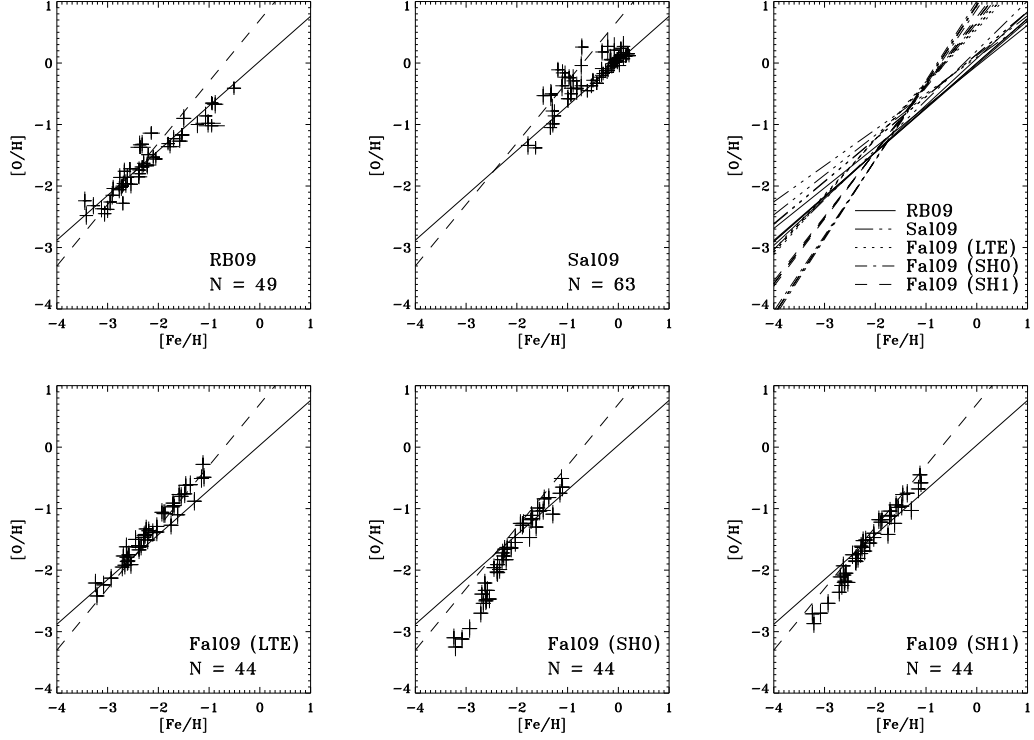


Figure 3: The $[O/H]$ - $[Fe/H]$ empirical relation deduced from two samples with heteroscedastic data, RB09 and Sal09, and three samples with homoscedastic data, Fal09, cases LTE, SH0, and SH1, indicated on each panel together with related population. Also plotted on each panel are the adopted linear dependences, $[O/H] = 0.72[Fe/H]$ (full) and $[O/H] = [Fe/H] + 0.70$ (dashed). The regression lines related to five different methods are shown for each sample on the top right panel. For further details refer to the text.

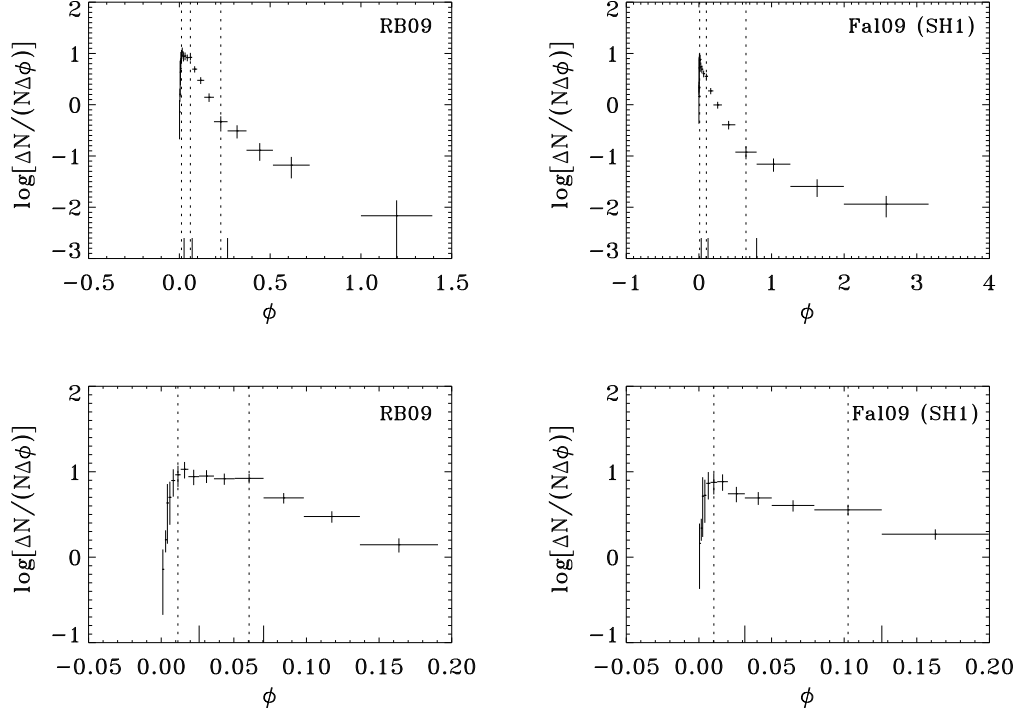


Figure 4: The empirical, differential oxygen abundance distribution (EDOD) related to the fs10 sample for $[\text{O}/\text{H}]-[\text{Fe}/\text{H}]$ empirical relations deduced from the RB09 (left panels) and Fal09, case SH1 (right panels) sample. The whole distribution is represented in upper panels, while lower panels zoom the low-metallicity range. The uncertainty of the distribution is determined from Poisson errors. The vertical bars on the horizontal axis mark $[\text{Fe}/\text{H}] = -2.2, -1.6, \text{ and } -0.8$. The vertical dotted lines mark $[\text{Fe}/\text{H}] = -2.7, -1.7, \text{ and } -0.9$, where the linear trend of the EDOD changes passing from a region to the adjacent one. For further details refer to the text.

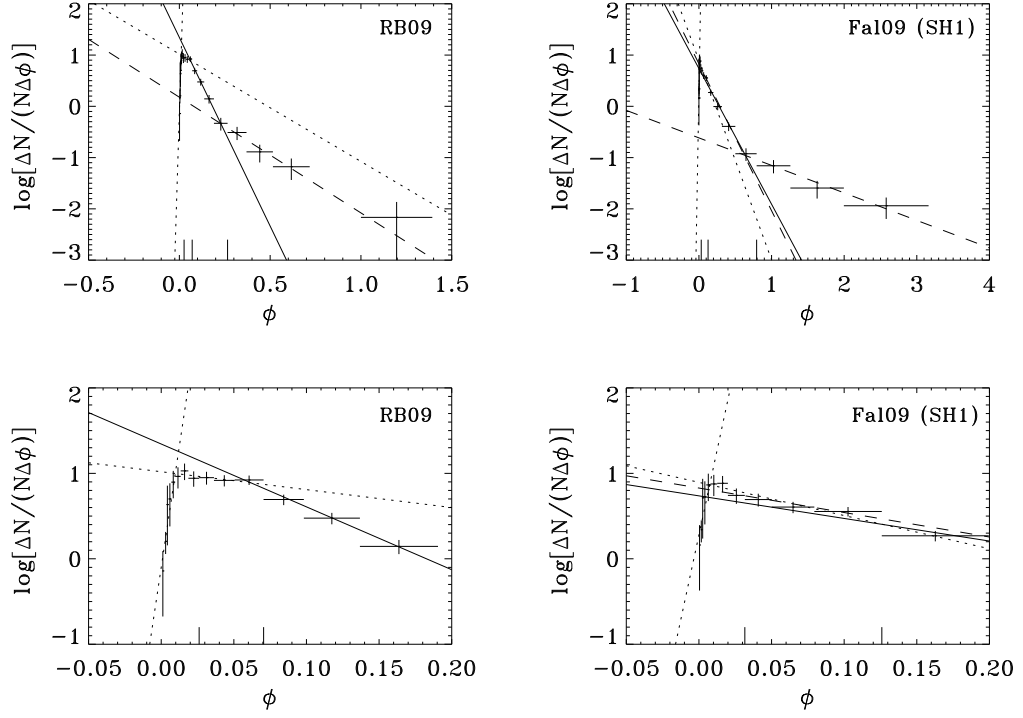


Figure 5: Regression lines to the empirical differential oxygen abundance distribution (EDOD) plotted in Fig. 4, with regard to the regions (from the left to the right): A (dotted, positive slope, $n_A = 6$), F (dotted, negative slope, $n_F = 6$), C (full, $n_C = 5$), E (dashed, $n_E = 4$). The more inclined dashed line on right panels corresponds to the FC ($n_{FC} = 10$) region, in alternative to F and C regions separately. Other captions as in Fig. 4. For further details refer to the text.